Digital noise reconstruction with a quantum sensor

by

Yuan Zhu

B.S., Physics
University of Science and Technology of China, 2019

Submitted to the Department of Nuclear Science and Engineering and
the Department of Electrical Engineering and Computer Science
in partial fulfillment of the requirements for the degrees
of
Master of Science in Nuclear Science and Engineering and
Master of Science in Electrical Engineering and Computer Science

at the

MASSACHUSETTS INSTITUTE OF TECHNOLOGY

May 2022

Author .....
Department of Nuclear Science and Engineering
Department of Electrical Engineering and Computer Science
May 8, 2022

Certified by .....
Paola Cappellaro
Korea Electric Power Professor of Nuclear Engineering
Professor of Nuclear Science and Engineering and Professor of Physics
Thesis Supervisor

Certified by .....
William D. Oliver
Professor of Electrical Engineering and Computer Science
Professor of Physics
Thesis Reader

Accepted by .....
Ju Li
Battelle Energy Alliance Professor of Nuclear Science and Engineering
and Professor of Materials Science and Engineering
Chair, Department Committee on Graduate Students

Accepted by .....
Leslie A. Kolodziejski
Professor of Electrical Engineering and Computer Science
Chair, Department Committee on Graduate Students

Digital noise reconstruction with a quantum sensor

by

Yuan Zhu

Submitted to the Department of Nuclear Science and Engineering and
the Department of Electrical Engineering and Computer Science
on May 8, 2022, in partial fulfillment of the
requirements for the degrees of
Master of Science in Nuclear Science and Engineering and
Master of Science in Electrical Engineering and Computer Science

Abstract

Interactions between a quantum system and its environment are usually inevitable and could lead to decoherence limiting the performance of quantum devices. On the one hand, to build robust quantum devices requires an in-depth characterization of such decoherence mechanism. On the other hand, the extracted environmental information brings us new approaches to investigate novel phases in quantum materials. Thus, probing and characterizing environmental noise is an essential task for both fundamental physics and quantum applications. Existing noise reconstruction methods in quantum systems rely on using approximated δ-like frequency filtering to sample the noise spectrum in frequency domain using dynamical decoupling sequences.

In this thesis, we propose a novel digital noise reconstruction method to reconstruct the environmental noise both in frequency and time domains, which avoids the δ-function approximation for frequency filtering. By measuring the decoherence of a qubit sensor under a set of Walsh modulation sequences, the (arithmetic) autocorrelation of a stationary Gaussian noise that couples to the quantum sensor is directly reconstructed and the corresponding noise spectrum is then reconstructed through linear transformations (discrete Fourier transform).

We systematically compare the typical dynamical decoupling-based noise reconstruction method (the Carr-Purcell- Meiboom-Gill reconstruction method) and the Walsh reconstruction method by evaluating the reconstruction errors of both methods under an Orstein-Unlenbeck noise model, which is commonly adopted to describe the magnetic noise generated by a dipolarly coupled spin bath. Combining theoretical and simulation results, we conclude that the accuracy of our Walsh reconstruction method is only limited by the time-space sampling and can be easily suppressed by increasing the reconstruction order.

We then perform a proof-of-principle demonstration using a single nitrogen-vacancy center in diamond to characterize its environmental noise dominated by the ^{13}C nuclear spin bath, and discuss the practical limitations of the reconstruction accuracy and avenues for its improvement. Finally we also introduce several directions of in-

terest for future research.

Thesis Supervisor: Paola Cappellaro
Title: Korea Electric Power Professor of Nuclear Engineering
Professor of Nuclear Science and Engineering and Professor of Physics

Thesis Reader: William D. Oliver
Title: Professor of Electrical Engineering and Computer Science
Professor of Physics

Acknowledgments

First of all, I would like to thank my supervisor Professor Paola Cappellaro. No matter what challenges I meet not only in research but also in life, she is the person who always guides me, encourages me, and supports me. Since I joined our research group, I have been continuously influenced by Paola's great passion and pure pursuit of scientific research. It is my great honor to be a part of the Quantum Engineering Group (QEG) under Paola's supervision.

I would like to thank my thesis reader Professor William Oliver for offering great, instructive and professional support throughout the thesis.

I would like to thank my amazing laboratory co-worker Guoqing Wang. We cannot make this "Walsh" project happen without Guoqing's patient guidance and "high-frequency" discussions.

Thank you to every QEG friend. Special thank you to Dianne Lior, Brandy Baker, Janet Fischer, Alicia Duarte, Alexandre Cooper, David Layden, Yixiang Liu, Calvin Won-Kyun Sun, Pai Peng, Changhao Li, Scott Alsid, Abtin Ameri and Boning Li.

I also want to thank every Promaxo friend I met in the summer of 2021, especially my manager Dinesh Kumar and my advisor Selin Chiragzada.

Thank you to every friend I have and will have in my life.

Particularly, I am very grateful to my families. It is my great fortune to being the daughter of my parents, to being the partner of Mr. Chen. Words alone are never enough to express my gratitude.

Last but not least, thank you to myself for being the unique girl who always believes in herself. It is a great pleasure for me to be an MIT student. Hope I will make MIT proud.

To my parents,
for loving and supporting me.

Contents

List of Figures

List of Tables

Chapter 1

Introduction

1.1 Outline of this thesis

Overall, this thesis studies a novel digital noise reconstruction method termed as *Walsh spectroscopy*, which utilizes a single qubit sensor subjected to spin flip control pulses at time locations given by Walsh sequences. In particular, it compares the Walsh reconstruction method with a representative of existing reconstruction methods based on Carr-Purcell-Meiboom-Gill (CPMG) sequences.

Chapter 2 introduces the background of typical noise spectroscopy methods based on dynamical decoupling control sequences, which are widely used in board research topics such as coherence protection. In Section 2.1, great efforts are put into the CPMG method, a general dynamical decoupling method which can be used to compare with the Walsh method in terms of the effects of noise reconstruction.

Section 2.1 is divided into three subsections. After a general introduction to the noise spectroscopy using a single qubit sensor system coupled to the time-dependent noise field, its accumulated phase under the dynamical decoupling sequence, resulted attenuation function of the system, as well as relation to the noise spectrum in the frequency domain are reviewed. In greater detail, Section 2.1.1 uses two commonly used dynamical decoupling methods - the periodic dynamical decoupling (PDD) method and the CPMG dynamical decoupling method to introduce the background of dynamical decoupling methods, to explicitly show their modulation dynamical decoupling

sequences, the expressions of their filter functions, and visualizations of state evolution by using the Bloch sphere. In Section 2.1.2, other interesting dynamical decoupling methods including XY, CDD, UDD and KDD are briefly discussed. In Section 2.1.3, noise spectroscopy based on the CPMG sequence is thoroughly discussed where the accuracy of the CPMG method is quantified.

Section 2.2 comprehensively introduces the Walsh reconstruction method with five subsections. In Section 2.2.1, we briefly overview the digital noise spectroscopy method we proposed based on Walsh sequences, termed as Walsh noise reconstruction. In Section 2.2.2, we formulize the entire Walsh operation chain as shown in Equation (2.52), where we start from the attenuation function measured by experiment, to obtain the noise auto-correlation function and spectrum through linear transformations. In Section 2.2.3, the transfer functions related to the aforementioned linear transformations in the Walsh operation chain (2.52) will be derived. In Section 2.2.4, we introduce details on the discrete Fourier transform for both the CPMG reconstruction method and the Walsh reconstruction method. In Section 2.2.5, we summarize the Walsh noise spectroscopy method.

Chapter 3 systematically compares the Walsh reconstruction method with the CPMG reconstruction method through simulation. We firstly introduce the noise model we use in our simulation in Section 3.1 given by the Ornstein-Uhlenbeck (OU) process, which is usually used for considering the characteristic spectrum of a spin qubit dipolarly coupled to spin bath [26]. Furthermore, in Section 3.3.1, we discuss the characteristics of the OU process such as its explicit expression in the discretized time series, auto-correlation and noise spectrum in theory. Then we define the metrics to quantify reconstruction errors in Section 3.2, which are preparations for our reconstruction comparison. We classify the metrics to quantify errors into two cases: the average error (Equation (3.7)) characterizing the overall reconstruction performance and the individual error (Equation (3.9)) characterizing time or frequency dependent reconstruction performance. Next, we show the simulation results and then analyze and draw conclusions from the results.

In Section 3.3, we present the reconstruction comparison between the CPMG and

Walsh reconstruction methods. In Section 3.3.1, we show an example of the comparison with the number of sequence $N = 32$ and sequence time length $T = 16$ μs. With a focus on Figure 3-2 and Figure 3-3, we clearly point out the advantages, disadvantages, and improvements of the Walsh method and the CPMG method respectively via simulation, and then summarize them in Table 3.1. In addition to the overall performance of the noise reconstruction discussed in Section 3.3.1, we then briefly look into the individual error of the two reconstruction methods in Section 3.3.2 and consequently draw conclusions from our simulation in Figure 3-4. Finally, in Section 3.4, we conduct a statistical analysis of the OU noise model to further understand the potential effects of insufficient numbers for averaging in practice or finite noise instances in this section and draw conclusions from Figure 3-5.

Chapter 4 shows the experimental demonstrations of both the Walsh reconstruction method or the CPMG reconstruction method. In our experiment, we use a single Nitrogen-vacancy (NV) center in the diamond sample as a quantum sensor to characterize its environmental noise dominated by ^{13}C nuclear spins. In Section 4.1, we briefly introduce the background on the NV center especially its application as a quantum sensor before we dive into experimental details. Then in Section 4.2 we show the comparison of the two methods in noise reconstruction. In Section 4.2.1, we introduce our homemade con-focal optical setup and electronic instruments we use in experiments (Figure 4-2). In Section 4.2.2, we perform the proof-of-principle demonstration of the Walsh reconstruction methods in Figure 4-3, where we also discuss the practical errors in experiment due to different factors and propose the avenues for their improvement accordingly.

Chapter 5 is the last part of this thesis. It summarizes the conclusions we drew from Chapter 2, Chapter 3 and Chapter 4, and propose several interesting topics we can conduct for future research based on the work in this thesis.

Chapter 2

Noise reconstruction with dynamical decoupling methods

Quantum sensing [14, 1, 55, 74, 15, 65, 17, 76, 28] utilizes the quantum properties of a quantum system to measure a physical quantity with high sensitivity [28]. Ideally, a perfectly isolated quantum system can maintain its coherence but cannot be manipulated [95], while an open quantum system interacts with the environment and can be affected by control fields but also by noise, which will induce the loss of coherence (we also call it decoherence [97, 75, 7]). There exist several methods to eliminate the decoherence, such as quantum error correction [42] and dynamical decoupling [92, 91, 90, 48, 94]. In this thesis, we focus on dynamical decoupling methods. Dynamical decoupling methods as powerful tools can not only reduce decoherence [86, 27, 51, 9, 69, 80], but also reconstruct the spectrum of stochastic signals, i.e. noise for open systems [28, 5, 13].

2.1 Noise spectroscopy with dynamical decoupling methods

In terms of how to actually use dynamical decoupling methods to reconstruct the noise spectrum, the answer is to apply π-pulse sequences. Dynamical decoupling

methods consist of single or multiple π-pulse sequences [96], which can be used to measure the on-resonance frequency components of the noise spectrum. By applying the sequence of pulses to modulate a quantum sensor and measuring its decoherence, the noise spectrum generated by quantum sensor-bath coupling can be reconstructed. Once the noise model is reconstructed, one can decouple the quantum system from its noisy environment by flipping the sign of the coupling and averaging the noise to zero, which means we can ideally have an open quantum system free from noise and decoherence.

The first developed dynamical decoupling protocol was the spin echo in nuclear magnetic resonance [39]. Figure 2-1 (a) shows a spin echo sequence, which is also called Hanh echo sequence, with a single π pulse applied at the middle of the time domain. Since then, more complex pulse-based sequences have been developed such as PDD sequences [28], CMPG sequences [28], XY sequences [34], etc.

Generally, for a single qubit (spin $S = \frac{1}{2}$) sensor coupled to time-dependent noise field $\omega(t)$, the Hamiltonian of the interaction between the qubit and bath resulting in dephasing [96] can be written as:

$$H_{SE} = \frac{\omega(t)}{2}\sigma_z, \tag{2.1}$$

where σ_z is one of the Pauli matrices defined in the z direction.

Assume we start with a qubit pure state $|0\rangle$. After applying a $\pi/2$ pulse, we can have a qubit initial state $|+\rangle = (|0\rangle + |1\rangle)/\sqrt{2}$. Each π pulse will make the spin flip once from its previous state (we will dive deeper into Section 2.1.1 with visualization of different sequences by demonstrating the spin state changes in Bloch sphere). Thereafter, during the free evolution time T, the accumulated phase $\phi(T)$ is:

$$\phi(T) = \int_0^T \omega(t) f(t) dt, \tag{2.2}$$

where time-dependent $f(t)$ is a dynamical decoupling modulation function with values alternating between $(+1)$ and (-1). Each time the function values change from $(+1)$ to (-1) or vice-versa, one (ideal) instantaneous π pulse with zero width is applied at

that switching moment.

The measurable population decay in state $|+\rangle$ $P_{|+\rangle}(T)$ which represents the qubit dephasing signal $S(T)$ can be written as:

$$\begin{aligned} S(T) &= P_{|+\rangle}(T) && (2.3)\\ &= \frac{1}{2}(1 + \langle\cos(\phi(T))\rangle) && (2.4)\\ &= \frac{1}{2}(1 + e^{-\chi}) && (2.5)\\ &= \frac{1}{2}(1 + e^{-\langle\phi^2\rangle/2}), && (2.6) \end{aligned}$$

where χ is the attenuation function. Such a formula is an average result after sufficient repetitions and here we assume the noise field is stationary, zero-mean, and Gaussian.

By analyzing the system in the rotating frame, the attenuation function χ of the system is then expressed as:

$$\chi = \frac{\langle\phi^2\rangle}{2} = \frac{1}{2}\int_0^T \int_0^T dt_1 dt_2 \langle\omega(t_1)\omega(t_2)\rangle f(t_1) f(t_2). \tag{2.7}$$

We define the auto-correlation function G (later on, G will be more accurately denoted as the arithmetic auto-correlation function) as:

$$G(t_1, t_2) = \langle\omega(t_1)\omega(t_2)\rangle, \tag{2.8}$$

which analyzes the correlation of the noise field with a delayed copy of itself in the time domain. Therefore, the attenuation function χ can be rewritten as:

$$\chi = \frac{\langle\phi^2\rangle}{2} = \frac{1}{2}\int_0^T \int_0^T dt_1 dt_2 G(t_1, t_2) f(t_1) f(t_2). \tag{2.9}$$

In particular, under the stationary and zero-mean Gaussian noise assumption, the auto-correlation G depends only on the time difference such that

$$G(t_1, t_2) = G(|t_1 - t_2|). \tag{2.10}$$

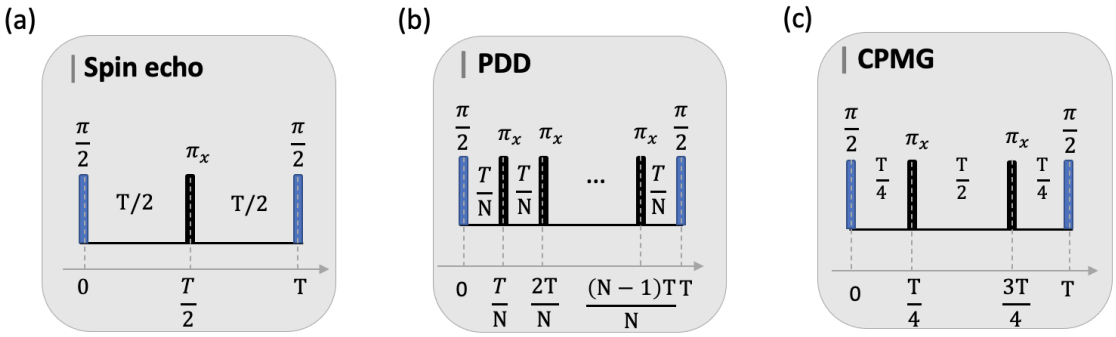

Figure 2-1: Examples of dynamical decoupling sequences and the total time period from 0 to T. (a) spin echo sequence; (b) PDD sequence; (c) the unit of CPMG sequence.

Note that, although in different experimental platforms the individual environmental noise source is likely to be non-Gaussian, the model we discuss here can still be a common approximation option if we have sufficient identical noise sources using the central limit theorem [35].

We also define a filter function $F(\omega)$ in the frequency domain as the Fourier transform over a time T of the dynamical decoupling modulation function $f(t)$ in the time domain:

$$F(\omega) = \int_0^T f(t) e^{i\omega t} dt, \tag{2.11}$$

where $F(\omega)$ has units of time (more details in Section 2.1.1). The attenuation function χ then can be expressed in the frequency domain as the overlap of the filter function generated by dynamical decoupling sequences and the real noise spectrum:

$$\chi = \frac{1}{2} \int_0^T \int_0^T dt_1 dt_2 f(t_1) f(t_2) \int_{-\infty}^{+\infty} \frac{d\omega}{2\pi} S(\omega) e^{i\omega(t_1 - t_2)} \tag{2.12}$$

$$= \frac{1}{2} \int_{-\infty}^{+\infty} \frac{d\omega}{2\pi} S(\omega) \left(\int_0^T f(t_1) e^{i\omega t_1} dt_1 \right) \left(\int_0^T f(t_2) e^{-i\omega t_2} dt_2 \right) \tag{2.13}$$

$$= \frac{1}{2} \int_{-\infty}^{+\infty} \frac{d\omega}{2\pi} S(\omega) |F(\omega)|^2. \tag{2.14}$$

2.1.1 Periodic dynamical decoupling method and Carr-Purcell-Meiboom-Gill method

As we mentioned earlier in Section 2.1, the simplest dynamical decoupling sequence is the spin echo sequence [39], where a single π pulse is applied at $T/2$ assuming the total time period is T, whose effectiveness relies on two underlying assumptions: (1) time-independent (static) noise; (2) ideally instantaneous with zero width (i.e. Dirac δ function) pulses [19].

Next, we introduce another two common multi-pulse dynamical decoupling methods, which are PDD and CPMG method via three main aspects including their modulation sequences, filter functions and visualizations of state evolution in the Bloch sphere.

Modulation sequences

As shown in Figure 2-1 (b), PDD [50] can be regarded as an extension of spin echo since it consists of $(N-1)$ π-pulses with the equal inter-pulse duration T/N over the total T period. Here, we assume all the π-pulses are applied along the x axis of Bloch sphere (will be introduced in detail in the "Visualizations of state evolution by using the Bloch sphere" part). In terms of the modulation sequence of CPMG [20] method, the unit of its sequence is shown in Figure 2-1 (c), where over the total T period, two π-pulses are applied separately at $T/4$ and $3T/4$. Therefore, for the N π-pulses CMPG sequence, the first π-pulse is applied at $T/2N$, the final π-pulse is applied at $(2N-1)T/2N$, and the remaining π-pulses are applied at $(1+2j)T/2N$ for $j = 1, \cdots, (N-2)$, and we have $N-1$ equally spaced inter-pulse duration T/N and the other 2 equally spaced duration $T/2N$. Note that N for CMPG method must be an even positive integer.

Filter functions

We have defined the general filter function as Equation (2.11) in Section 2.1. Next, we derive the filter function for PDD modulation sequence first. For a $(N-1)$ π-pulses

PDD with its pulse interval T/N, its filter function $F_{PDD}(\omega)$ can be calculated as:

$$|F_{PDD}(\omega)|^2 = |\int_0^T f_{PDD}(t)e^{i\omega t}dt|^2 \tag{2.15}$$

$$= \frac{4\sin^2(\frac{N(\pi+\omega\tau)}{2})\tan^2(\frac{\omega\tau}{2})}{\omega^2} \tag{2.16}$$

$$= \frac{4\sin^2(\frac{N\omega\tau}{2})\tan^2(\frac{\omega\tau}{2})}{\omega^2} \tag{2.17}$$

$$= \frac{4\sin^2(\frac{N\omega\tau}{2})\sin^2(\frac{\omega\tau}{2})}{\omega^2\cos^2(\frac{\omega\tau}{2})}. \tag{2.18}$$

Second, we derive the filter function for CPMG modulation sequence. For a N π-pulses CPMG with its pulse interval T/N, its filter function $F_{CPMG}(\omega)$ can be calculated as:

$$|F_{CPMG}(\omega)|^2 = |\int_0^T f_{CPMG}(t)e^{i\omega t}dt|^2 \tag{2.19}$$

$$= \frac{16\sin^2(\frac{N\omega\tau}{2})\sin^4(\frac{\omega\tau}{4})}{\omega^2\cos^2(\frac{\omega\tau}{2})}, \tag{2.20}$$

where N is an even integer.

Example of filter functions with specific numerical values for PDD and CPMG are shown in Figure 2-2.

Visualizations of state evolution by using the Bloch sphere

First, we introduce what the Bloch sphere is. The Bloch sphere is a representation of the state space available to qubits. Every pure state of a qubit is a point on the surface of the Bloch sphere. In Figure 2-3, a pure arbitrary state can be defined by two parameters θ and ϕ as:

$$|\psi\rangle = \cos\frac{\theta}{2}|0\rangle + e^{i\phi}\sin\frac{\theta}{2}|1\rangle. \tag{2.21}$$

Any point on the sphere can be transformed via a unitary transformation to another point on the sphere, which means any pure state can transform to another pure state via a unitary transformation on the Bloch sphere.

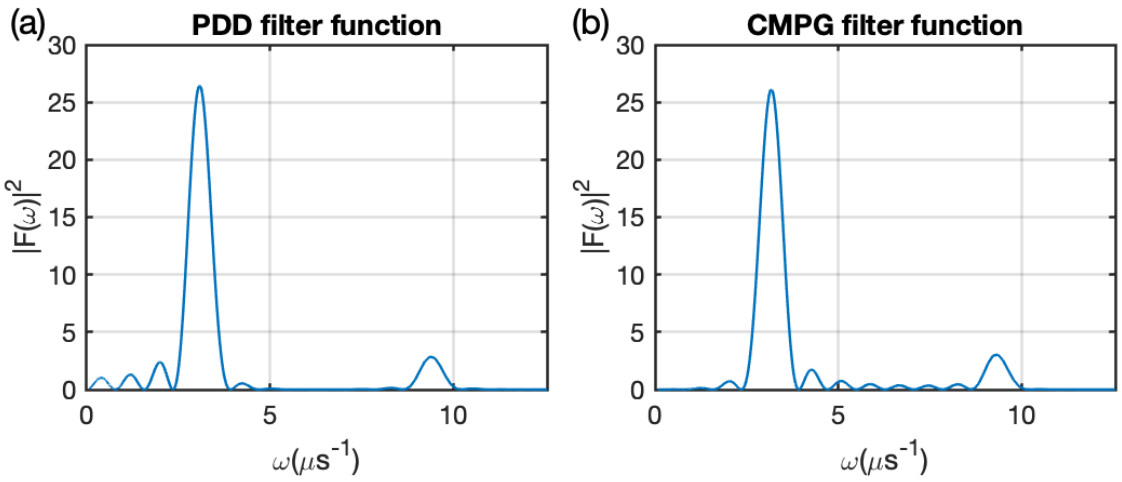

Figure 2-2: An example of PDD filter function and CPMG filter function for $N = 8$, $\tau = 1$ μs [19]. (a) PDD filter function; (b) CPMG filter function.

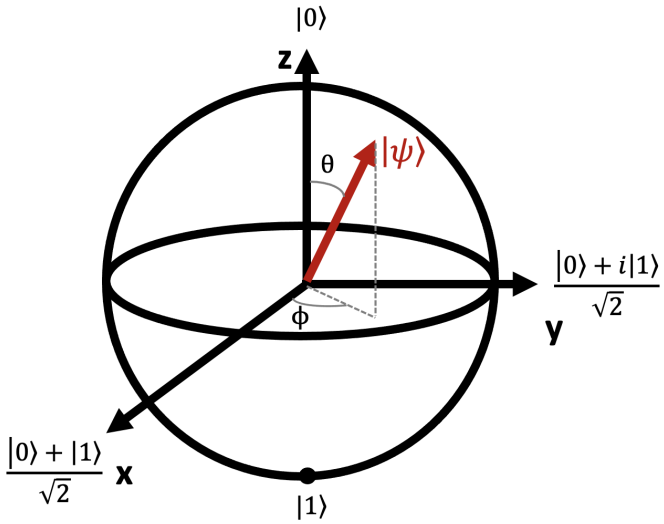

Figure 2-3: The Bloch sphere is a 3D sphere with a radius of 1. A state can be well regarded as a point in or on the surface of the Bloch sphere. If the state is a pure state, it will be a point on the surface and can be explicitly written as an expression of two parameters θ and ϕ while the others can be represented as points inside the Bloch sphere. In addition, in this Figure, we can find that the states $|0\rangle$ and $|1\rangle$ are both on the z axis, and the states $\frac{|0\rangle+|1\rangle}{\sqrt{2}}$ and $\frac{|0\rangle-|1\rangle}{\sqrt{2}}$ are both on the x axis, and the states $\frac{|0\rangle+i|1\rangle}{\sqrt{2}}$ and $\frac{|0\rangle-i|1\rangle}{\sqrt{2}}$ are both on the y axis.

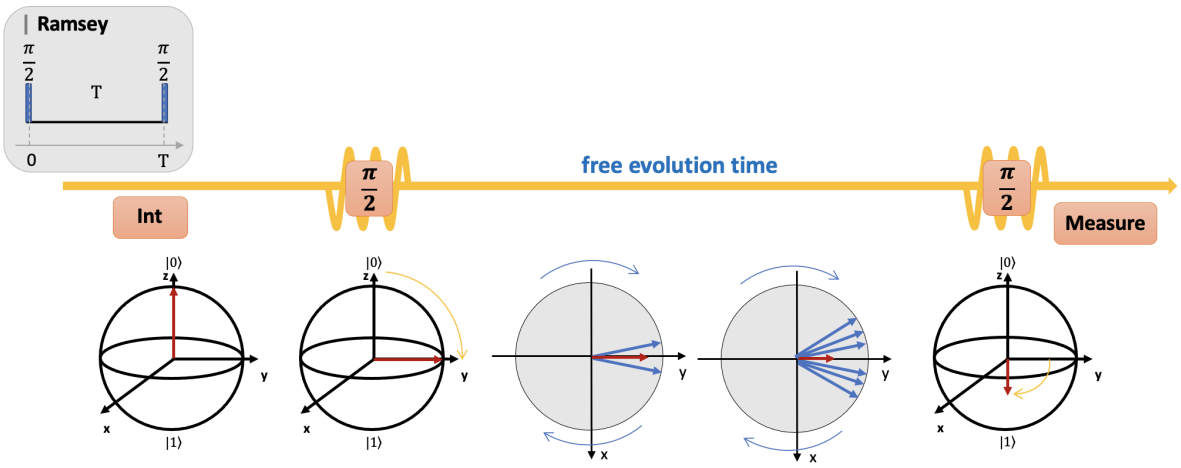

Figure 2-4: Visualization of a Ramsey sequence. Each sphere is a Bloch sphere. The red arrow represents the averaged state of repeated experiments and each blue arrow represents a state after a single experiment evolution

We then can visualize the state evolution from its pure state $|0\rangle$ to its initial state $|+\rangle$ shown in Figure 2-4 by adding a $\pi/2$ pulse. On the Bloch sphere, to add a $\pi/2$ pulse along the x axis means to rotate the vector representing the pure state $|0\rangle$ 90° around the x axis. Therefore, the pure state $|0\rangle$ is transformed to the initial state $|+i\rangle$ shown in the y axis with a radius 1.

Figure 2-4 represents the evolution process of a qubit state with a Ramsey sequence, where no π-pulse is added. Therefore, the evolution of the initial state is free and random. As shown in the third and fourth Bloch spheres, each blue arrow represents the potential evolution of a state and the red arrow represents the averaged state of repeated experiments. After the other $\pi/2$-pulse added at the end of the time period T, the final state is inside the Bloch sphere which means at this moment, the state is not a pure state any more. By measuring the population decay along z axis, we then can derive the attenuation function χ based on the dephasing signal with Ramsey experiments.

Figure 2-5 represents the evolution process of a qubit state with a spin echo sequence. The initialization is the same as the Ramsey sequence. After applying a $\pi/2$-pluse, we can obtain the pure initial state $|+i\rangle$. During the time period from

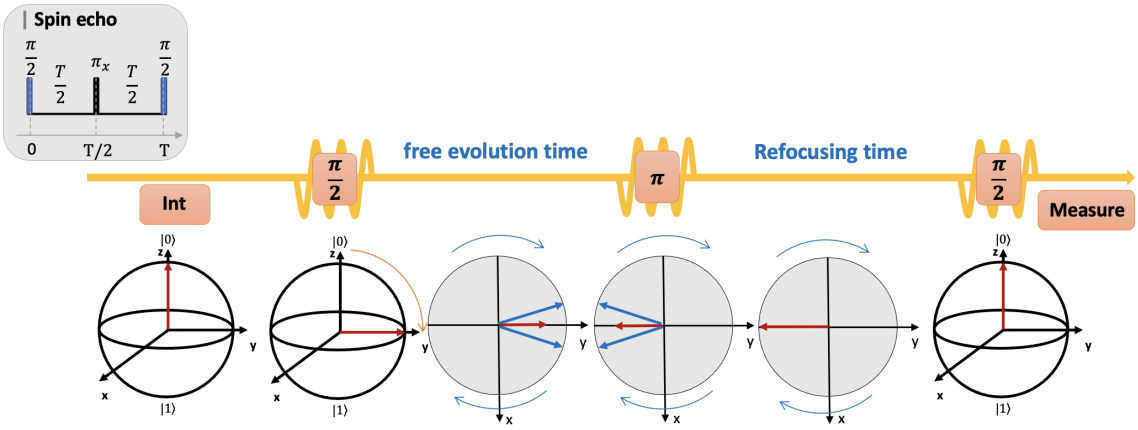

Figure 2-5: Visualization of a spin echo sequence. A π-pulse is applied at $t = T/2$, which makes the free evolution become refocusing evolution.

$t = 0$ to $t = T/2$, the evolution is still the same as the Ramsey free evolution period. However, by applying a π-pulse at $t = T/2$ along y axis, the evolution of the states in each experiment can offset its first $T/2$ period effect and refocus back to a pure state which is symmetric compared to the initial state $|+i\rangle$ and can be denoted as $|-i\rangle$. Therefore, after the other $\pi/2$-pulse, ideally we can obtain a final pure state $|0\rangle$ and the decay should be zero. However, in real experiments, the sequences can be imperfect with finite pulse widths and pulse errors, and people have developed various kinds of dynamical decoupling modulation sequences to cancel these effects.

Figure 2-6 represents the evolution process of a qubit state with a general and arbitrary dynamical decoupling sequence. As shown in Figure 2-6, multi-π pulses modulation sequences can finally make the measurable decay signal as:

$$P(|0\rangle) = \langle \cos^2(\frac{\phi}{2}) \rangle. \tag{2.22}$$

with ϕ defined as an accumulated phase:

$$\phi(T) = \int_0^T \omega(t) f(t) dt, \tag{2.23}$$

where $\omega(t)$ is a time-dependent noise field and $f(t)$ is a modulation function corresponding to a pulse sequence.

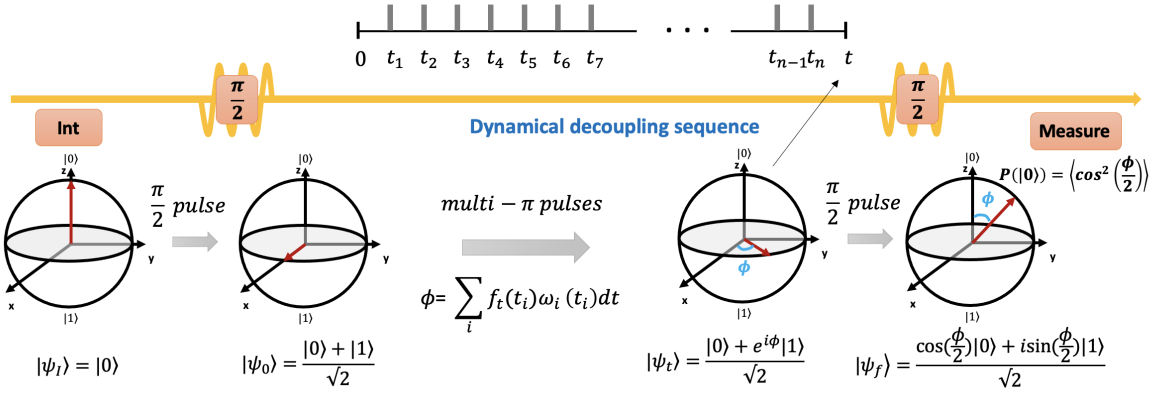

Figure 2-6: Visualization of a general dynamical decoupling sequence. In total, n π-pulses are applied independently at $t = t_1, t = t_2, \cdots, t = t_{n-1}, t = t_n$. Therefore, during the evolution time with a dynamical decoupling sequence, the phase ϕ has been accumulated, which will reflect on the final measurement of the $|0\rangle$ state population as a function of the phase ϕ.

2.1.2 Other dynamical decoupling methods

In addition to the spin echo methods, the PDD methods, the CPMG methods, there are also some other general dynamical decoupling methods such as the concatenated dynamical decoupling (CDD) methods, the Uhrig dynamical decoupling (UDD) methods, the Knill dynamical decoupling (KDD) methods, and XYs dynamical decoupling method [80, 4, 2, 34, 98, 77, 69, 53]. We will discuss them in the remaining part of this section.

However, one to note here is that, under most circumstances, we only use the CPMG dynamical decoupling sequences and the XYs dynamical decoupling sequences in noise spectroscopy. In this thesis, we will only work on the comparison between the CPMG reconstruction method and the Walsh reconstruction method.

XYs dynamical decoupling method

As indicated in the name of the XYs method [38, 58], it effect makes a state rotate along both x and y axis, i.e. its π-pulses are applied as π_x and π_y corresponding to π rotations around the σ_x and σ_y operators for the qubit [34]. The XYs method requires the total number of π-pulses is the multiple of 4. The XYs methods are

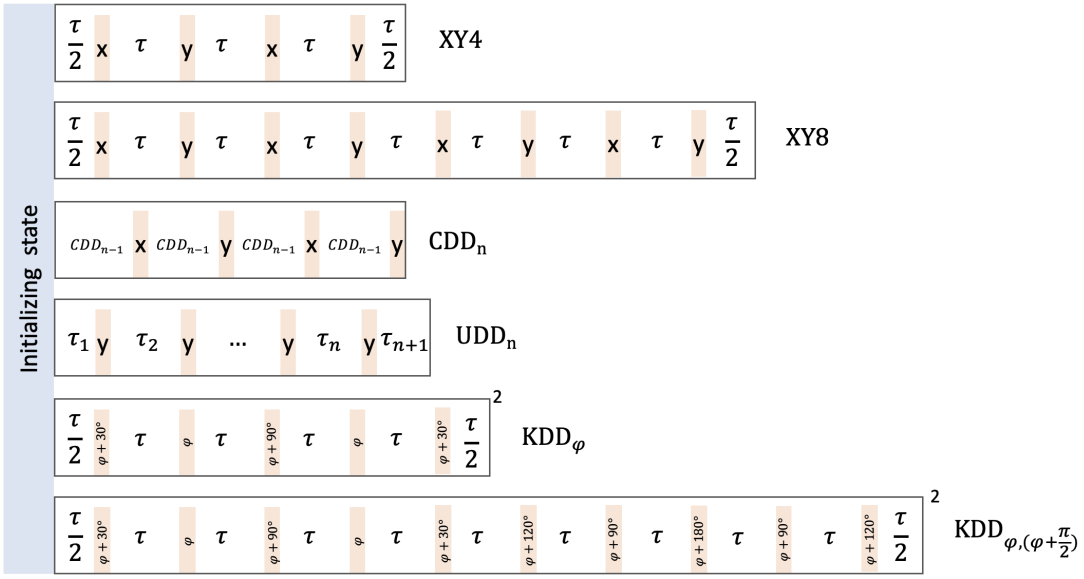

Figure 2-7: Other dynamical decoupling sequence schemes including XY4, XY8, CDD_n, UDD_n, KDD_φ, and $\mathrm{KDD}_{\varphi,(\varphi+\frac{\pi}{2})}$ [4, 2, 34, 80].

designed to reduce the effects of π-pulse imperfections [2]. There are two main XYs methods that have been commonly used, which are called the XY4 method [61] and the XY8 method [2, 34], and their dynamical decoupling sequence schemes are shown in Figure 2-7 respectively and can be explicitly written as:

$$XY4 = (\frac{\tau}{2})\pi_x(\tau)\pi_y(\tau)\pi_x(\tau)\pi_y(\frac{\tau}{2}), \tag{2.24}$$

where τ is a given time interval;

and

$$XY8 = (\frac{\tau}{2})\pi_x(\tau)\pi_y(\tau)\pi_x(\tau)\pi_y(\tau)\pi_x(\tau)\pi_y(\tau)\pi_x(\tau)\pi_y(\frac{\tau}{2}), \tag{2.25}$$

where τ is a given time interval.

Concatenated dynamical decoupling method

As indicated in the name of the CDD method, it is concatenated recursively. That means, for the CDD method, as shown in Figure 2-7, its sequence scheme with n pulses depends on the sequence scheme with $(n-1)$ pulses where its sequence with

one single pulse is a PDD sequence, i.e. $CCD_{n=1} = PDD$. The explicit recursive relation of CCD_n and $CCD_{(n-1)}$ with $n > 1$ can be written as:

$$CCD_n = (CCD_{n-1})\pi_x(CCD_{n-1})\pi_y(CCD_{n-1})\pi_x(CCD_{n-1})\pi_y, \tag{2.26}$$

where π_x and π_y are π-pulses applied along x direction and y direction of the Bloch sphere [4].

Compared to the PDD methods, theoretically, the CDD methods perform better "asymptotic superiority" when the number of π-pulses is finite [48], and experimentally, the CDD methods are more robust when it comes to pulse errors, which means less oscillation pattern will be observed [4].

Uhrig dynamical decoupling method

For UDD method, as shown in Figure 2-7, its sequence scheme with n pulses has $(n+1)$ time intervals $\tau_1, \cdots, \tau_{n+1}$, which are defined by:

$$\tau_j = \tau_c(\sin^2(\frac{j\pi}{2(n+1)}) - \sin^2(\frac{(j-1)\pi}{2(n+1)})), \tag{2.27}$$

where $j = 1, \cdots, (n+1)$, τ_c is the total time [4, 88, 89]. Therefore, the UDD sequence scheme can be explicitly written as:

$$UDD_n = (\tau_1)\pi_y(\tau_2)\pi_y \cdots (\tau_n)\pi_y(\tau_{n+1}), \tag{2.28}$$

where π_y represents a π-pulse applied along y direction of the Bloch sphere, or rather, a state rotates along its y axis for 180° [4].

The UDD method is designed to minimize the interaction between system and environment with specific n π-pulses [4, 88, 89] and it has been proved to behave best to eliminate the decoupling of system due to its interaction with environment in the low frequency region [25, 4, 88, 89]. As shown in the experimental part of Ref. [4], the UDD methods perform similarly compared to the CPMG methods in terms of decay time.

Knill dynamical decoupling method

For KDD methods, as shown in Figure 2-7, its sequence scheme is:

$$KDD_{\varphi} = ((\tau/2)\pi_{\varphi+\frac{\pi}{6}}(\tau)\pi_{\varphi}(\tau)\pi_{\varphi+\frac{\pi}{2}}(\tau)\pi_{\varphi}(\tau)\pi_{\varphi+\frac{\pi}{6}}(\tau/2))^2, \tag{2.29}$$

where φ denotes the rotation axis as $(\sigma_x \cos\varphi + \sigma_y \sin\varphi)$ [77], and τ is a given time interval. Note here the power of 2 means to repeat the same sequence twice. In particular, when the rotation axis is x axis, the sequence scheme of KDD_x can be written as:

$$KDD_{x} = ((\tau/2)\pi_{x+\frac{\pi}{6}}(\tau)\pi_{x}(\tau)\pi_{x+\frac{\pi}{2}}(\tau)\pi_{x}(\tau)\pi_{x+\frac{\pi}{6}}(\tau/2))^2. \tag{2.30}$$

To better improve the robustness of the sequence, people also extend KDD_{φ} to $(KDD_{\varphi} + KDD_{\varphi+\frac{\pi}{2}})$ by applying a $\pi/2$ phase shift, which can be written as:

$$KDD_{\varphi,(\varphi+\frac{\pi}{2})} = ((\frac{\tau}{2})\pi_{\varphi+\frac{\pi}{6}}(\tau)\pi_{\varphi}(\tau)\pi_{\varphi+\frac{\pi}{2}}(\tau)\pi_{\varphi}(\tau)\pi_{\varphi+\frac{\pi}{6}}(\tau)\pi_{\varphi+\frac{2\pi}{3}}(\tau)\pi_{\varphi+\frac{\pi}{2}}(\tau)\pi_{\varphi+\pi}(\tau)\pi_{\varphi+\frac{\pi}{2}}(\tau)\pi_{\varphi+\frac{2\pi}{3}}(\frac{\tau}{2}))^2. \tag{2.31}$$

Therefore, in particular, the KDD_{xy} sequence scheme can be written as:

$$KDD_{xy} = ((\frac{\tau}{2})\pi_{x+\frac{\pi}{6}}(\tau)\pi_{x}(\tau)\pi_{x+\frac{\pi}{2}}(\tau)\pi_{x}(\tau)\pi_{x+\frac{\pi}{6}}(\tau)\pi_{x+\frac{2\pi}{3}}(\tau)\pi_{x+\frac{\pi}{2}}(\tau)\pi_{x+\pi}(\tau)\pi_{x+\frac{\pi}{2}}(\tau)\pi_{x+\frac{2\pi}{3}}(\frac{\tau}{2}))^2 \tag{2.32}$$

$$= ((\frac{\tau}{2})\pi_{x+\frac{\pi}{6}}(\tau)\pi_{x}(\tau)\pi_{x+\frac{\pi}{2}}(\tau)\pi_{x}(\tau)\pi_{x+\frac{\pi}{6}}(\tau)\pi_{y+\frac{\pi}{6}}(\tau)\pi_{y}(\tau)\pi_{y+\frac{\pi}{2}}(\tau)\pi_{y}(\tau)\pi_{y+\frac{\pi}{6}}(\frac{\tau}{2}))^2. \tag{2.33}$$

The KDD methods are the most robust dynamical decoupling methods used to correct two specific pulse errors - off-resonance errors and flip-angle errors which are the dominant two types of errors in many experimental cases [77, 34].

2.1.3 Noise spectroscopy with the Carr-Purcell-Meiboom-Gill reconstruction method

Overview of the CPMG method

CPMG sequence is the most common modulation sequence used in recent years to reconstruct noise spectrum [28]. We will discuss the reconstruction by using the CPMG method in this section. As we discussed in Section 2.1.1, the filter function of a CPMG sequence with N π-pulses with inter-pulse duration τ is Equation (2.20). This filter function can be approximated for large T as a weighted sum over a series of Dirac δ functions [96], which can be written as:

$$|F_{CPMG}(\omega)|^2 = \frac{16\sin^2(\frac{N\omega\tau}{2})\sin^4(\frac{\omega\tau}{4})}{\omega^2\cos^2(\frac{\omega\tau}{2})} \tag{2.34}$$

$$\approx \sum_{k=0}^{\infty}\frac{8T}{\pi^2}\frac{1}{(2k+1)^2}\delta(\omega-\frac{(2k+1)\pi}{\tau}). \tag{2.35}$$

Therefore, $|F(\omega)|^2$ have peak values at $\omega = (2k+1)\pi/\tau$ where k is an arbitrary integer. The attenuation function χ of CPMG sequences can be re-calculated and simplified approximately by the following steps:

$$\chi = \frac{1}{2}\int_{-\infty}^{+\infty}\frac{d\omega}{2\pi}S(\omega)|F_{CPMG}(\omega)|^2 \tag{2.36}$$

$$\approx \frac{1}{\pi}\int_{-\infty}^{+\infty}d\omega\frac{S(\omega)}{\omega^2}\frac{N\tau\pi}{2}\frac{1}{(\frac{\tau}{2})^2}\sum_{k=-\infty}^{+\infty}\delta(\omega-\frac{(2k+1)\pi}{\tau}) \tag{2.37}$$

$$= T\frac{4}{\pi^2}\sum_{k=0}^{+\infty}\frac{1}{(2k+1)^2}S(\frac{(2k+1)\pi}{\tau}), \tag{2.38}$$

where we make use of the symmetric relation of the noise spectrum $S(\omega) = S(-\omega)$ and apply the δ-function approximation to the above calculation process:

$$\int_{-\infty}^{+\infty}\frac{\sin^2(ax)}{x^2}dx = a\pi, \quad \frac{\sin^2(ax)}{x^2}|_{a\to\infty} = a\pi\delta(x). \tag{2.39}$$

From Equation (2.38), we can conclude that the attenuation χ is mainly influenced by the components of noise spectrum at the resonance frequency π/τ and also its odd harmonics $(2k+1)\pi$ for k is positive integers, where the effects of harmonics decreases as k increases due to the corresponding weighted item $1/(2k+1)^2$ for each k. Therefore, the main component of noise spectrum $S(\pi/\tau)$ can be reconstructed. More accurately, the noise spectrum $S(\omega)$ can be reconstructed by varying the value of inter-pulse duration τ in Equation (2.38) [96].

An example to better understand noise spectroscopy beforehand

To better understand the noise spectroscopy by using the CPMG method, we can first look into the Ramsey example [54, 28]. For a Ramsey sequence, we can easily calculate its filter function as:

$$|F(\omega)|^2 = \frac{4\sin^2(\frac{\omega T}{2})}{\omega^2}. \tag{2.40}$$

Then, we can derive the relation between the attenuation factor of Ramsey and its noise spectrum as:

$$\chi_{Ramsey} = \frac{1}{\pi}\int_{-\infty}^{+\infty} \frac{\sin^2(\frac{\omega T}{2})}{\omega^2} d\omega \tag{2.41}$$

$$\approx \frac{1}{\pi}\int_{-\infty}^{+\infty} \frac{T\pi}{2}\delta(\omega)S(\omega)d\omega \tag{2.42}$$

$$= \frac{T}{2}S(0). \tag{2.43}$$

Telling from Equation (2.43), since the attenuation factor χ_{Ramsey} is measurable, the component of noise spectrum $S(0)$ can be well reconstructed.

Accuracy of noise spectroscopy using the CPMG method

As we discussed above, the accuracy of noise spectroscopy heavily relies on the approximation to the Dirac comb structure of the filter function and correspondingly is limited by the requirement of a large T. Intuitively telling from Figure 2-2, when

$N = 8$, the PDD and CPMG filter functions cannot be ideally regarded as a pure delta function centered on a single frequency since there are some small peaks around it and the width of the main peak is non-zero while the CPMG based filter function is closer to an ideal delta function compared to the PDD one. From Ref.[82], we can obtain the attenuation factor χ in the time domain written as:

$$\chi = \chi_1 + \chi_2, \tag{2.44}$$

where

$$\chi_1 = T \sum_m |c_m|^2 \int_0^T dt(1 - \frac{t}{T}) G(|t|) e^{im\omega_p t}, \tag{2.45}$$

and

$$\chi_2 = \sum_{m_1 \neq -m_2} \frac{c_{m_1} c_{m_2}}{(m_1 + m_2)\omega_p} \int_0^T G(|t|)(e^{im_1\omega_p t} - e^{-im_2\omega_p t}), \tag{2.46}$$

where $c_m = \frac{1}{T}\int_o^T e^{-im\omega_p t} f(t) dt$ is the Fourier component of the filter function at frequency $m\omega_p$, and $\omega_p = \frac{2\pi}{T}$ and $f(t) = \sum_m c_m e^{im\omega_p t}$ $(0 \leq t \leq T)$, therefore both c_{m1} and c_{m2} are well defined. Now, the attenuation factor χ is split into two parts, the first term is a linear function of T and we call it the "diagonal" term; the second term is the remaining off-diagonal term so that we call it the "off-diagonal" term. For a large T in comparison to the noise correlation time τ_c, both the "off-diagonal" term and t/T part of the "diagonal" term in Equation (2.44) can be neglected.

Therefore, in particular, for a CPMG sequence with a large T compared to the noise correlation time τ_c, we can have its attenuation factor χ_{CPMG} as:

$$\chi_{CPMG} = T \sum_{k=0}^{\infty} |c_k|^2 S(\frac{(2k+1)\pi}{\tau}), \tag{2.47}$$

where

$$|c_k|^2 = \frac{16\sin^4(\frac{m\omega_p\tau}{4})\sin^2(\frac{\omega_p N\tau}{2})}{m^2\omega_p^2T^2\cos^2(\frac{m\omega_p\tau}{2})}|_{m=2k+1} \tag{2.48}$$

$$= \frac{4\sin^2(kN\pi)}{(2k+1)^2\pi^2N^2\sin^2(k\pi)} \tag{2.49}$$

$$= \frac{4}{\pi^2}\frac{1}{(2k+1)^2}, \tag{2.50}$$

where $\omega_p = \pi/\tau$, and $m = (2k+1)$, $k = 0, 1, 2, \cdots$ are odd numbers because of the symmetric structure of CPMG sequences, which is consistent with Equation (2.38).

However, the approximation treating the filter function as a Dirac δ comb requires that the noise spectrum around the resonance frequencies has a small variation with respect to the peak width of the filter function for a reasonable approximation. The same argument in time-space states that the sequence time T has to be much larger than the noise correlation time τ_c. In Ref. [82], a precise analysis gives a relative error of the calculated attenuation function using the δ approximation as

$$\left|\frac{\Delta\chi(T)}{\chi(T)}\right| \sim \frac{\tau_c(1-e^{-\frac{T}{\tau_c}})}{T}. \tag{2.51}$$

Although such an error can be suppressed by simply increasing the sequence time T, sometimes the coherence time of the quantum system is not long enough for a high-fidelity measurement with large T, and increasing the sequence time T also degrades the sensitivity and efficiency of noise reconstruction. In addition, the experiment apparatus might have limited resources for implementing a long sequence. Therefore, it is important to find a more accurate and efficient way to reconstruct the noise, even in time space which relates to the spectrum simply through a Fourier transformation.

2.2 Walsh reconstruction method

Rather than reconstructing the noise spectrum by applying periodic dynamical decoupling sequences such as CPMG sequences and approximating the filter function with δ functions, the Walsh method uses a complete set of digital filters applied by

non-periodic Walsh modulation sequences to reconstruct the auto-correlation of noise in the time domain, which is intrinsically compatible with the sequence control and time discretization [41, 23, 59].

The story of the Walsh reconstruction method begins from the Walsh matrix, which is a $2^n \times 2^n$ square matrix (n is a positive integer) with elements either 1 or -1. Each row of the Walsh matrix is orthogonal to another and represents a pulse sequence that will generate a pulse whenever an element of the row changes its sign compared to the last element. Take $n = 3$ as a simple example, we can get a 8×8 Walsh matrix as:

$$\begin{pmatrix} 1 & 1 & 1 & 1 & 1 & 1 & 1 & 1 \\ 1 & 1 & 1 & 1 & -1 & -1 & -1 & -1 \\ 1 & 1 & -1 & -1 & -1 & -1 & 1 & 1 \\ 1 & 1 & -1 & -1 & 1 & 1 & -1 & -1 \\ 1 & -1 & -1 & 1 & 1 & -1 & -1 & 1 \\ 1 & -1 & -1 & 1 & -1 & 1 & 1 & -1 \\ 1 & -1 & 1 & -1 & -1 & 1 & -1 & 1 \\ 1 & -1 & 1 & -1 & 1 & -1 & 1 & -1 \end{pmatrix}.$$

According to what we have discussed above, the first row is a Ramsey sequence, the second is a spin echo sequence, the third is a unit CPMG sequence, the fourth is a PDD sequence, the fifth is another CPMG sequence, and the eighth is another PDD sequence with a twice shorter period compared to the fourth one, while the sixth and the seventh sequences are not typical dynamical decoupling sequences and they are unique sequences components in Walsh sequence series when $n = 3$.

Since the Walsh reconstruction method is based on a combination of sequences (we call it Walsh modulation sequences, or Walsh sequences) instead of a single sequence, its filter function is a combination of the corresponding filter functions. For $n = 2$, we can have the Walsh sequence as well as the Walsh filter function as shown in Figure 2-8.

By using the Walsh method, the noise spectrum can be reconstructed through three independent linear transforms starting from Walsh power spectrum χ [73]. First,

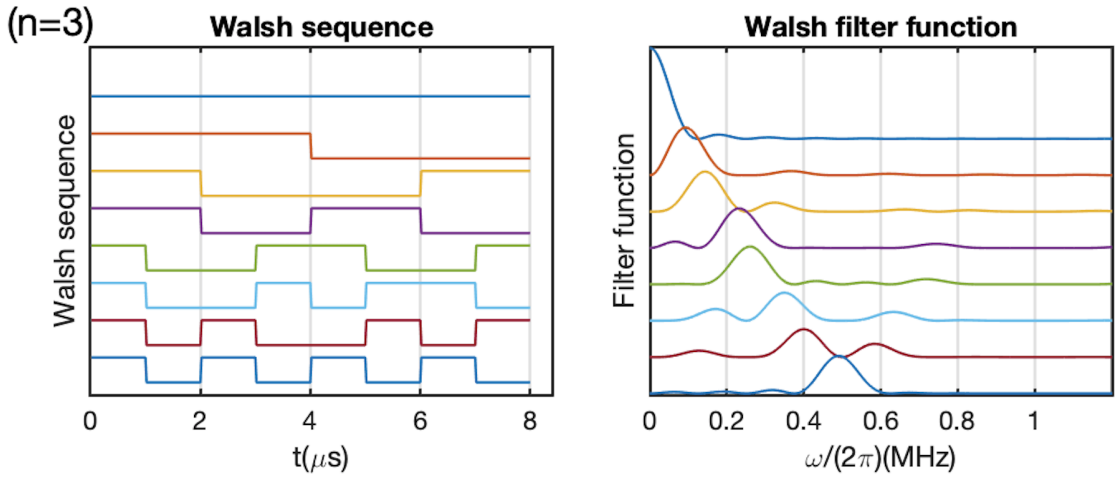

Figure 2-8: An example of Walsh sequence with $n = 3$ (i.e. $N = 8$) and $T = 8$ μs and its corresponding filter function.

we can get the logical auto-correlation function L [73] by applying the inverse Walsh transform to χ. Second, the arithmetic auto-correlation function G [73] can be derived by applying the transfer matrix T_{L-A} to the logical auto-correlation function L. Third, the noise spectrum $S(\omega)$ is the inverse Fourier transform of the the arithmetic auto-correlation function G. Therefore, we have the following chain of operations:

$$P_W \xrightarrow{W^{-1}} L \xrightarrow{T_{L-G}} G \xrightarrow{F^{-1}} S(\omega), \tag{2.52}$$

where the Walsh power spectrum P_W shown in the chain (2.52) can be obtained through the attenuation function as $P_W = \frac{2\chi}{T^2}$ and χ can be directly obtained directly from experiments (Section 4.2).

Note that the arithmetic auto-correlation function is now usually directly called the auto-correlation function. Also note that the logical auto-correlation of the noise is derived based on the "logical" Wiener-Khintchine theorem [73]. As a reminder, we have derived the attenuation function χ at the beginning of Chapter 2 as Equation (2.9).

2.2.1 Overview of discrete Walsh reconstruction method

Since in practical experiments we will obtain a discrete sampling of the correlation function, our model is based on a discrete version. To explicitly present the procedure of Walsh reconstruction method, here we define the time discretization and express the transformations in the matrix form. The continuous time period T is discretized in N equal time intervals $\frac{T}{N}$. The m^{th} Walsh modulation functions $y_m(t)$ are chosen from the m^{th} row of the $N \times N$ Walsh matrix. The discretized logical and arithmetic auto-correlation functions are $L_N(j) \equiv L(\frac{jT}{N})$, $G_N(j) \equiv G(\frac{jT}{N})$ for $j = 0, \cdots, N-1$. Then, similarly as we discussed in the continuous time domain, we can follow the steps for noise spectroscopy in the discrete time domain:

1. measure χ_m under the Walsh modulation function $y_m(t)$ for $m = 1, \cdots, N$;
2. derive the discrete logical auto-correlation $L_N(k)$ for $k = 1, \cdots, N$;
3. derive the discrete arithmetic auto-correlation $G_N(j)$ for $j = 1, \cdots, N$;
4. derive the discrete noise spectrum $S(\omega)$.

2.2.2 Detailed derivation of discrete Walsh reconstruction method

In greater detail, the attenuation χ_m can be calculated as:

$$\chi_m = \frac{1}{2}\int_0^T \int_0^T dt_1 dt_2 G(t_1 - t_2) y_m(\frac{t_1}{T}) y_m(\frac{t_2}{T}) \tag{2.53}$$

$$= \frac{T^2}{2N^2} \sum_{k,j} \bar{G}_N(j-k) W_m(j) W_m(k) \tag{2.54}$$

$$\approx \frac{T^2}{2N^2} \sum_{k,j} G_N(j-k) W_m(j) W_m(k), \tag{2.55}$$

where $W_m(j)$ is the discretized m^{th} Walsh modulation function and corresponds to the value of $y_m(\frac{t}{T})$ at $t \in (\frac{(j-1)T}{N}, \frac{jT}{N}]$. Moreover, here, we define $\bar{G}_N(j-k)$ as:

$$\bar{G}_N(j-k) = \frac{N^2}{T^2} \int_{\frac{(k-1)T}{N}}^{\frac{kT}{N}} \int_{\frac{(j-1)T}{N}}^{\frac{jT}{N}} dt_1 dt_2 G(t_1 - t_2), \tag{2.56}$$

which can be approximated by $G_N(j-k)$ and $G_N(j-k) = G(\frac{(j-k)T}{N})$.

The relation between the attenuation χ and the arithmetic auto-correlation function G_N has been introduced in Equation (2.55). However, from the format of the function:

$$G_N(j-k) = G(\frac{(j-k)T}{N}) = \langle \omega(\frac{jT}{N})\omega(\frac{kT}{N})\rangle = \langle \omega_N(j)\omega_N(k)\rangle, \tag{2.57}$$

we cannot directly and linearly transform the measured attenuation χ to the arithmetic auto-correlation function G_N to get the final reconstructed noise spectrum $S(\omega)$. Therefore, we introduce and define the logical auto-correlation function L_N for the discretized noise $\omega(j)$ as [73]:

$$L_N(j) = \frac{1}{N}\sum_{k=1}^{N}\langle \omega(k)\omega(k \oplus j)\rangle, \tag{2.58}$$

where $\oplus$ denotes the bit-by-bit modulo 2 addition of two numbers j and k and the reason why we use bitwise binary modulo is that the Walsh sequences are defined under the binary basis [wiki walsh]. As defined in Equation (2.58), we can have:

$$L_N(j) = \frac{1}{N}\sum_{k=1}^{N}\langle \omega(k)\omega(k \oplus j)\rangle = \frac{1}{N}\sum_{k=1}^{N} G_N(j \oplus k - k), \tag{2.59}$$

which shows that the transform from the logical auto-correlation function L_N to the arithmetic auto-correlation function G_N is linear. In order to tell the relation between the measured attenuation χ_m and the logical auto-correlation function L_N, we recall Equation (2.55) and Equation (2.59). By altering j to $j \oplus k$ and applying the dyadic composition $W_m(j)W_m(k) = W_m(j \oplus k)$, $\forall j, k \in \mathcal{N}$ as well to Equation (2.55), we

have:

$$\chi_m \approx \frac{T^2}{2N^2} \sum_{k,j\oplus k} G_N(j \oplus k - k) W_m(j \oplus k) W_m(k), \tag{2.60}$$

$$= \frac{T^2}{2N^2} \sum_{k,j\oplus k} G_N(j \oplus k - k) W_m((j \oplus k) \oplus k), \tag{2.61}$$

$$= \frac{T^2}{2N^2} \sum_{j} (\sum_{k} G_N(j \oplus k - k)) W_m(j), \tag{2.62}$$

$$= \frac{T^2}{2N} \sum_{j} L_N(j) W_m(j)., \tag{2.63}$$

which shows that the logical auto-correlation L_N can be derived from the measured attenuation χ_m. Therefore, by repeating our experiment with a series of N Walsh functions, we can reconstruct the local auto-correlation L_N.

Now, we have showed the linear transforms from measured attenuation χ_m, to logical auto-correlation function L_N, and to arithmetic auto-correlation function G_N. However, as shown in Equation (2.59), we are not able to interpret L_N in terms of physical parameters, and currently, we only have the definition of L_N in a dyadic format instead of in the real time domain, which leads to the difficulty to reconstruct G_N from L_N since $u = t_1 - t_2$ and $v = t_1 \oplus t_2$ belong to different integration spaces.

2.2.3 Transfer functions

In order to solve the problem stated above, we introduce a bi-linear transfer function T_N [73] and a diagonal matrix D_N [73] to convert the arithmetic auto-correlation function G_N that is expressed in the discrete time domain where $t_1 - t_2 = \frac{(j_1 - j_2)T}{N}$ to the logical auto-correlation function L_N that is expressed in the dyadic domain where $t_1 \oplus t_2 = \frac{j_1 T}{N} \oplus \frac{j_2 T}{N}$.

The bi-linear transfer matrix T_N can be recursively generated by following:

$$T_N = \begin{pmatrix} T_{N/2} & 0 \\ T_{N/2} S_{N/2} & T_{N/2} \end{pmatrix}, \tag{2.64}$$

where S_N is so called the $N \times N$ shuffling matrix [73] with unit elements "off to the right of the SW-NE diagonal" and we have $S_1 = 0$ and $T_1 = 1$. To further get a glance of the bi-linear transfer matrix T_N in detail, since $S_1 = 0$ and $T_1 = 1$, we can derive T_2 based on the definition:

$$T_2 = \begin{pmatrix} T_1 & 0 \\ T_1 S_1 & T_1 \end{pmatrix}, \tag{2.65}$$

$$= \begin{pmatrix} 1 & 0 \\ 0 & 1 \end{pmatrix}. \tag{2.66}$$

Then based on T_2 we get above and $S_2 = \begin{pmatrix} 0 & 0 \\ 0 & 1 \end{pmatrix}$, we can get T_4 as:

$$T_4 = \begin{pmatrix} T_2 & 0 \\ T_2 S_2 & T_2 \end{pmatrix}, \tag{2.67}$$

$$= \begin{pmatrix} 1 & 0 & 0 & 0 \\ 0 & 1 & 0 & 0 \\ 0 & 0 & 1 & 0 \\ 0 & 1 & 0 & 1 \end{pmatrix}. \tag{2.68}$$

Then based on T_4 we get above and $S_4 = \begin{pmatrix} 0 & 0 & 0 & 0 \\ 0 & 0 & 0 & 1 \\ 0 & 0 & 1 & 0 \\ 0 & 1 & 0 & 0, \end{pmatrix}$, we can get T_8, and then T_{16}, T_{32}, et al.

The diagonal matrix defined as D_N can be generated with $D_N(k,k) = 2^{1-\delta(k,0)-V_k}$ where $\delta(k,0) = 1$ if and only if k=0, V_k is the number of ones of k represented in the binary format [73].

Now, we have explained the methods to numerically and recursively construct both the bi-linear transfer function $T_N(k,j)$ and the diagonal matrix $D_N(k,k)$, such

that:

$$L_N(k) = D_N(k,k) \sum_j T_N(k,j) G_N(j). \tag{2.69}$$

Therefore, we have:

$$G_N(j) = \sum_k T_N^{-1}(k,j) D_N^{-1}(k,k) L_N(k), \tag{2.70}$$

where T_{L-G} shown in the chain (2.52) corresponds to $T_N^{-1} D_N^{-1}$ here.

Since the arithmetic auto-correlation function G is even-symmetric about the origin, i.e. $G(t) = G(-t)$, we can also assume the discretized arithmetic auto-correlation function G_N satisfies a similar equation $G_N(j) = G_N(-j)$ for $j = 1, \cdots, N$. Then, by using discrete Fourier transform (as a reminder, DFT will be discussed in Section 2.2.4), we can reconstruct the discretized noise spectrum $S(\omega_k)$ with a set of discretized frequencies $\omega_k = \frac{Nk\pi}{(N-1)T}$ where $k = 0, \cdots, (N-1)$.

2.2.4 Discrete Fourier transform

Since the reconstructed Walsh auto-correlation are values of $G(t)$ in the discrete time domain and CPMG spectrum are values of $S(\omega)$ in the discrete frequency domain rather than the mean value in each of the time or frequency piece, here we will slightly modify the discrete Fourier transform to make it compatible with our protocols and to give less errors than existing fast Fourier transform functions such as the "fft" functions in MATLAB®.

For the noise reconstruction with the Walsh method using $N = 2^n$ sequences with time T, we first obtain the discrete values of the auto-correlation $G(t_j)$ with $t_j = 0, \frac{T}{N}, \cdots, \frac{T(N-1)}{N}$ where correspondingly $j = 0, 1, \cdots, (N-1)$. With the assumption of a symmetric auto-correlation such that $G(-t) = G(t)$, we can extend the time range and obtain $(2N-1)$ points of discrete $G(t_j)$ with $t_j = jT/N$, $j = -(N-1), \cdots, 0, \cdots, (N-1)$. The corresponding discrete Fourier frequency components we can obtain is then $S(\omega_k)$ with $\omega_k = \frac{\pi k}{T(N-1)/N}$ where $k = 0, \cdots, N-1$, which can be

calculated as

$$S(\omega_k) = \int_{-\infty}^{\infty} G(t) e^{-i\omega_k t} dt \tag{2.71}$$

$$\approx \sum_{j=-(N-1)}^{N-1} G(t_j) e^{-i\pi \frac{k}{T(N-1)/N} \frac{jT}{N}} \Delta t \tag{2.72}$$

$$= \sum_{j=-(N-1)}^{N-1} G(t_j) e^{-i\pi \frac{kj}{N-1}} \Delta t \tag{2.73}$$

where $\Delta t = T/N$.

2.2.5 Summary of discrete Walsh reconstruction method

To sum up, based on the operational chain (2.52), we can reconstruct the noise spectrum by using Walsh modulation functions and a series of different linear transformation correspondingly in practice with following steps:

1. measure χ_m under the Walsh modulation function $y_m(t)$ for $m = 1, \cdots, N$;

2. calculate the discrete logical auto-correlation $L_N(k)$ for $k = 1, \cdots, N$ based on

$$L_N(k) = \frac{2N}{T^2} \sum_m W_N^{-1}(k, m) \chi_m; \tag{2.74}$$

3. calculate the discrete arithmetic auto-correlation $G_N(j)$ for $j = 1, \cdots, N$ based on Equation (2.70);

4. calculate the discrete noise spectrum $S(\omega)$ by applying the discrete Fourier transform of the arithmetic auto-correlation G_N based on Equation (2.73).

Chapter 3

Comparison between the Walsh reconstruction method and the Carr-Purcell-Meiboom-Gill reconstruction method

As we discussed in Section 2, before our work, only the CPMG dynamical decoupling sequences and the XYs dynamical decoupling sequences were used in noise spectroscopy. Considering the numbers of π-pulses in Walsh sequences of the Walsh reconstruction method are not always the multiples of 4, in this thesis and our real work, we will only conduct the comparison between the CPMG reconstruction method and the Walsh reconstruction method.

In this chapter, we will first introduce the noise model - the Ornstein–Uhlenbeck (OU) process we use with aspects of its history and its key characteristics in Section 3.1, and second introduce the metric in our work to quantify the reconstruction errors including both the average error and the individual error in Section 3.2, and then show the simulation results and corresponding analysis to compare the CPMG reconstruction method and the Walsh reconstruction method in Section 3.3, and finally under the framework of the metrics we introduce and develop in Section 3.2,

demonstrate the statistical analysis of the OU process in Section 3.4.

3.1 Noise model – the Ornstein-Uhlenbeck process

Different noise models such as Gaussian noise model, white noise model and Poisson-Gaussian noise model, etc., have been developed to interpret and understand unavoidable noise in different circumstances [16].

In particular, the OU process, named after Leonard Salomon Ornstein and George Eugene Uhlenbeck, is a Gauss-Markov stochastic process [87, 3]. The OU model has a lot of applications in diverse areas such as mathematical finance [21, 56], physics [12] and biology [60, 45]. In terms of the applications specifically in physics, the velocity of massive Brownian particles with the impact of friction [33] can be modeled the OU process and it is also the original physics application of the OU process model. Most significantly, the characteristic spectrum of a spin qubit dipolarly coupled to a spin bath also can be described by OU process [26], which is exactly the model we use for noise modeling and simulation in this thesis.

3.1.1 Characteristics of the Ornstein-Uhlenbeck process

In Ref. [36, 37], the time trace of the OU noise $\omega(t)$ was defined as:

$$\omega(t+dt) = \omega(t)e^{-\frac{dt}{\tau_c}} + r\sqrt{b^2(1-e^{-\frac{2dt}{\tau_c}})}, \tag{3.1}$$

where τ_c characterizes the correlation time, b^2 represents the strength of the noise, and r is a random number following a standard normal distribution. We only consider the discrete OU process, which means that we have a time step Δt regarded as the smallest time interval we can address. Therefore, the time-dependent noise field $\omega(t)$ of the OU noise can be traced as:

$$\omega(t+\Delta t) = \omega(t)e^{-\frac{\Delta t}{\tau_c}} + r\sqrt{b^2(1-e^{-\frac{2\Delta t}{\tau_c}})}. \tag{3.2}$$

In addition,the OU noise $\omega(t)$ has an auto-correlation:

$$G(t) = \langle \omega(t)\omega(0) \rangle = b^2 e^{-\frac{t}{\tau_c}}. \tag{3.3}$$

Correspondingly, the noise spectrum is then written as:

$$S(\omega) = \int_{-\infty}^{\infty} dt (G(t)e^{-i\omega t}) = \int_{-\infty}^{\infty} dt (b^2 e^{-\frac{|t|}{\tau_c}}) e^{-i\omega t} = \frac{2b^2\tau_c}{1+\omega^2\tau_c^2} \tag{3.4}$$

which is a Lorentzian spectral line shape.

Furthermore, as for the noise source with a nonzero frequency shift ω_s such that the corresponding noise spectrum is modified to:

$$S_{\omega_s}(\omega) = \frac{b^2\tau_c}{1+(\omega-\omega_s)^2\tau_c^2} + \frac{b^2\tau_c}{1+(\omega+\omega_s)^2\tau_c^2}. \tag{3.5}$$

Its auto-correlation function is modified to the formula as:

$$G_{\omega_s}(t) = \langle \omega(t)\omega(0) \rangle = b^2 e^{-\frac{t}{\tau_c}} \cos(\omega_s t). \tag{3.6}$$

Again, in the following analysis parts of this chapter, we will continue to use the OU process as the noise model.

3.2 Metrics to quantify reconstruction errors

We have discussed how to reconstruct noise spectrum with the CPMG reconstruction method and the Walsh reconstruction method in Section 2.2.4. Next, we will discuss how to quantify reconstruction errors and then apply the metric to compare the errors generated in the CPMG method process and the Walsh method process respectively.

In Section 3.2.1, we will recall the different processes of the Walsh reconstruction method and the CPMG reconstruction method, and then establish the criteria we need to develop the metrics to quantify errors. In Section 3.2.2, we will not only introduce our metric to quantify the reconstruction average errors but also explain

why the other commonly used average error metric does not work here. Finally, in Section 3.2.3, we will discuss the individual metric we use to quantify errors.

3.2.1 Overview of the metrics to quantify errors

Errors will be introduced when the discrete Fourier transform is actually applied in noise spectroscopy instead of Fourier transform. In order to evaluate the reconstruction in both time and frequency domains, we make them comparable through proper normalization. Herein, we define two metrics to quantify the average error and the individual error during the noise reconstruction process.

3.2.2 The metric to quantify the average error

For a reconstructed noise parameter O and its corresponding theoretical value O_0 (here O can be either noise spectrum $S(\omega)$ in frequency domain or arithmetic noise auto-correlation $G(t)$ in time domain), we define the average error as:

$$\epsilon(O) = \frac{\sum_i (O(i) - O_0(i))^2}{\sum_i (O_0(i))^2}. \tag{3.7}$$

Another commonly used metric to quantify the average error can be written as:

$$\epsilon(O) = \sum_i \frac{(O(i) - O_0(i))^2}{(O_0(i))^2}. \tag{3.8}$$

However, in our case, we cannot guarantee that, for each i which represents a point we analyze, each $O_0(i)$ will be nonzero. Therefore, if there exists a theoretical zero value of $O_0(i)$, we then will not be able to normalize the errors of each individual reconstructed point, and correspondingly the average error cannot be well defined. Therefore, we use the metric defined in Equation (3.7) to quantity the average error.

3.2.3 The metric to quantify the individual error

In addition, to discuss the error of noise reconstruction in different frequency or time regions, we can define the error for an individual reconstructed point as:

$$E(O(i)) = \left| \frac{(O(i) - O_0(i))}{O_0(i)} \right|, \tag{3.9}$$

which is similar and comparable to the definition of the attenuation χ error in Ref. [82].

3.3 Simulation results and analysis

On the basis of the OU noise model, we will discuss the comparison between the Walsh reconstruction method and the typical dynamical decoupling - CPMG reconstruction method.

In this Section 3.3, we will first demonstrate the metric that we exclusively develop to compare the two reconstruction methods and secondly look into the errors raised by the two methods numerically and analytically in Section 3.3.1 with a focus on Figure 3-2 and Figure 3-3. Then, in Section 3.3.2, different from the view of the average errors discussed in Section 3.3.1, we will briefly elaborate the individual errors led by the two reconstruction methods respectively.

3.3.1 Reconstruction comparison between the Carr-Purcell-Meiboom-Gill method and the Walsh method with the average error

In order to make a fair comparison, the first and last sequences for the CPMG reconstruction method are designed to sample the same frequencies as the Walsh reconstruction method such that the ranges of reconstructed spectrum $S(\omega)$ and auto-correlation $G(t)$ are the same as (or very similar to) the Walsh reconstruction method. In addition, the total sequence time $\sim NT$ for both methods should also be similar to each other. More precisely, the first sequence of CPMG scheme is a

Ramsey sequence with $f(t) = 1$, and the $2k, (2k+1)$ sequences are both CPMG-k sequences with pulse interval $\tau_{2k} = T/(2k-1)$, $\tau_{2k+1} = T/(2k)$ respectively, where the values of k go from 1 to $N/2$. Such a set of CPMG sequences gives a sampling in the frequency domain $\omega_k = k\pi/T$ with $k = 0, \cdots, N$. Assume a symmetric spectrum such that $S(-\omega) = S(\omega)$. Then we can extend the frequency range and obtain discretized $S(\omega_k)$ with $2N+1$ points $\omega_k = -\frac{\pi N}{T}, \cdots, -\frac{\pi}{T}, 0, \frac{\pi}{T}, \cdots, \frac{\pi N}{T}$ where $k = -N, \cdots, 0, \cdots, N$. The corresponding discretized auto-correlation we can obtain is then $G(t_j)$ with $t_j = \frac{jT}{N}$ where $j = 0, \cdots, N$, which can be calculated as

$$G(t_j) = \frac{1}{2\pi} \int_{-\infty}^{\infty} S(\omega) e^{i\omega t_j} d\omega \tag{3.10}$$

$$\approx \frac{1}{2\pi} \sum_{k=-N}^{N} S(\omega_k) e^{i\pi \frac{k}{T} \frac{jT}{N}} \Delta\omega \tag{3.11}$$

$$= \sum_{k=-N}^{N} S(\omega_k) e^{i\pi \frac{kj}{N}} \frac{\Delta\omega}{2\pi}. \tag{3.12}$$

An example of the comparison with $N = 32$ and $T = 16$ μs is shown in Figure 3-1. In Figure 3-1, to compare the CPMG reconstruction method and the Walsh reconstruction method, the sequence time T is fixed, the sampling of these two methods in time and frequency domains are very similar. To maintain the same centers of peak positions in the filter functions which are calculated as $|F(\omega)|^2 = |\int f(t) e^{-i\omega t} dt|^2$, the only slight differences between these two methods happen in the CPMG-$2k$ sequences compared to the Walsh-$2k$ sequences where $k = 1, \ldots, 8$. In this example, the total sequence time for the Walsh method is 16×16 μs $= 256$ μs, while the total sequence time for the CPMG method is 256 μs + $(\frac{16}{1} + \frac{16}{3} + \cdots + \frac{16}{15})$ μs ≈ 288 μs, which is around 12.6% longer.

At this moment, we have developed a metric to compare the Walsh reconstruction method and the CPMG reconstruction method. Next, we will look into the simulation results and draw conclusions about the two methods in terms of reconstruction and errors (average errors discussion in this Section 3.3.1 and individual errors discussion in the next Section 3.3.2).

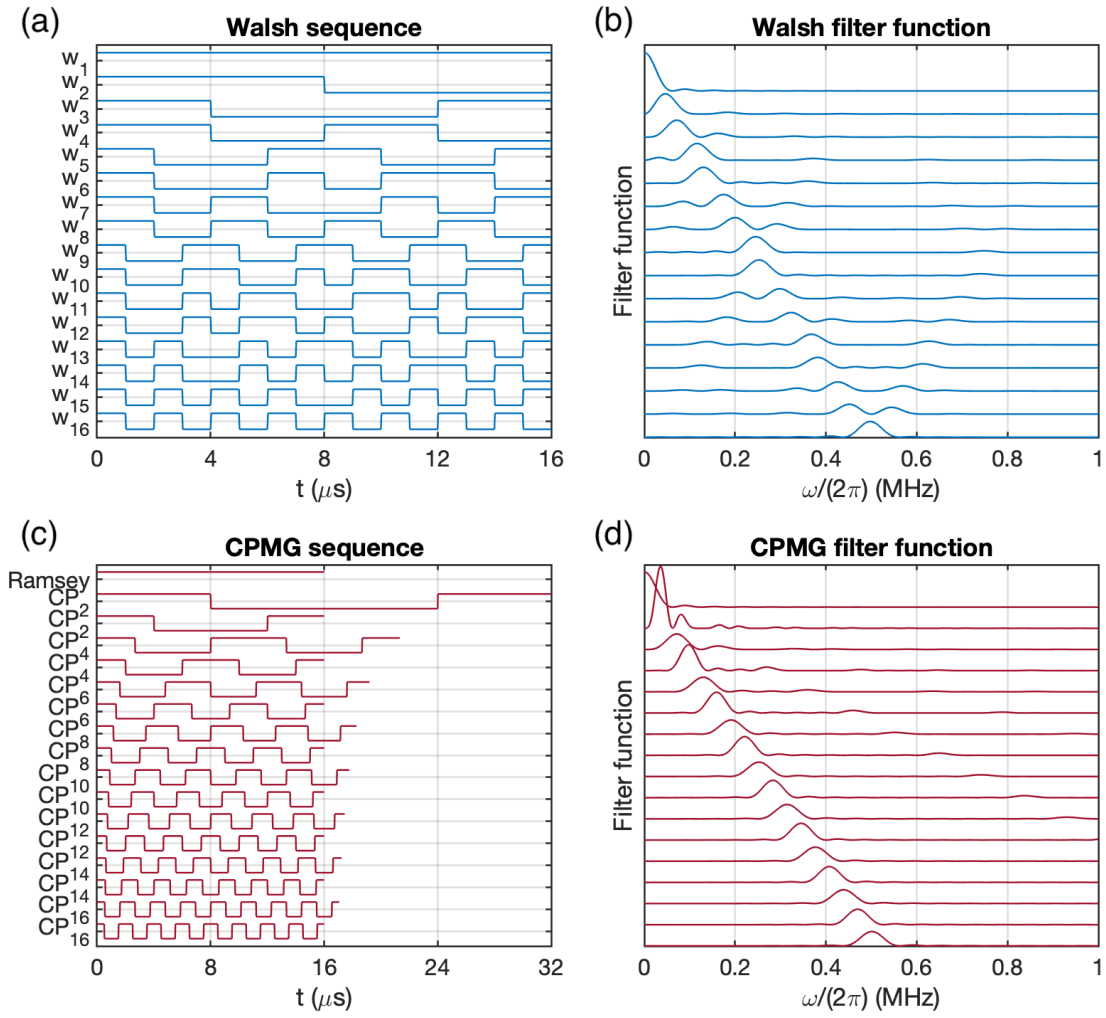

Figure 3-1: An example of the comparison by using the Walsh and CPMG sequences respectively when $N = 32$ and $T = 16$ μs. The filter functions in both (b) and (d) are calculated as $|F(\omega)|^2 = |\int f(t)e^{-i\omega t}dt|^2$.

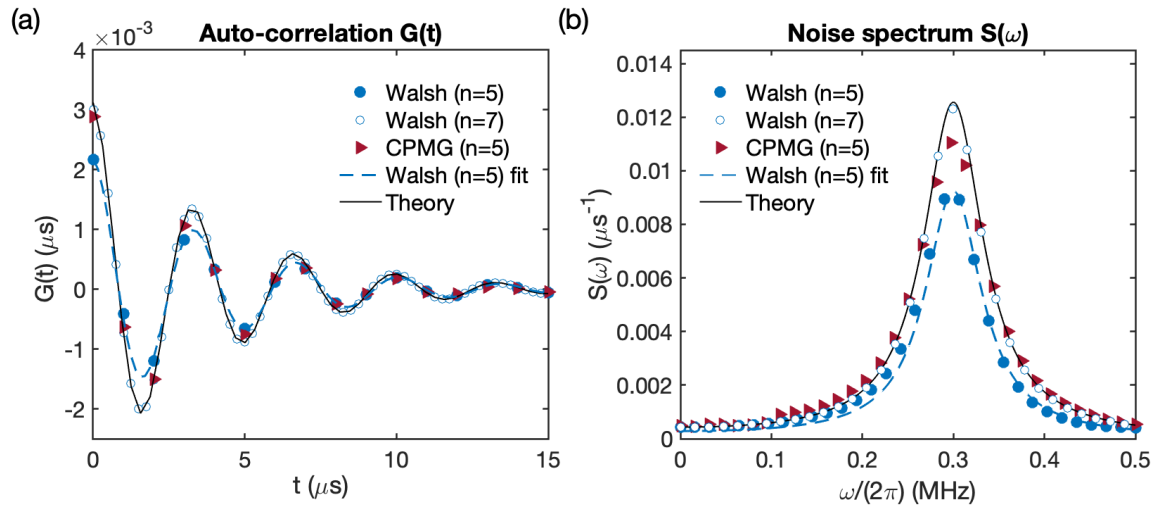

Figure 3-2: (a) Arithmetic auto-correlation reconstruction. The OU noise parameters we set here are $\tau_c = 4$ μs, $b^2 = 0.003125$ μs, $\omega_s = (2\pi)0.3$ MHz. The sequence time for both Walsh method and CPMG method is $T = 32$ μs. To better visualize the comparison, data is shown only from 0 to 15 μs. (b) Noise spectrum reconstruction with the same parameters as (a). The "Walsh fit" plots Equation (3.5) with the fitting value of b^2, τ_c, ω_s from the corresponding arithmetic auto-correlation data in (a).

We consider the noise satisfying an OU model with a non-zero frequency shift ω_s and the correlation time denoted as τ_c. In our simulation, the OU noise parameters we set are $\tau_c = 4$ μs, $b^2 = 0.003125$ μs, $\omega_s = (2\pi)0.3$ MHz and the sequence time for both of the Walsh method and the CPMG method is $T = 32$ μs. Figure 3-2 and Figure 3-3 fully include the corresponding simulation results. The inset (a) of Figure 3-2 shows the arithmetic auto-correlation $G(t)$ reconstruction. To better visualize the comparison, data is shown only from 0 to 15 μs because the differences among all sets of data become minor after 10 μs. Both the Walsh method and the CPMG method can well reconstruct the the arithmetic auto-correlation $G(t)$. As shown in the (a), when n is larger changing from $n = 5$ to $n = 7$, the Walsh method can perform $G(t)$ reconstruction better. The inset (b) of Figure 3-2 shows the noise spectrum $S(\omega)$ reconstruction. When n is relatively small ($n = 5$), the CPMG method reconstructs the noise spectrum $S(\omega)$ better than the Walsh method. However, when n becomes relatively larger ($n = 7$), the reconstruction of $S(\omega)$ via the Walsh method can be significantly improved.

To better interpret the effects mentioned in Figure 3-2, we simulate and obtain

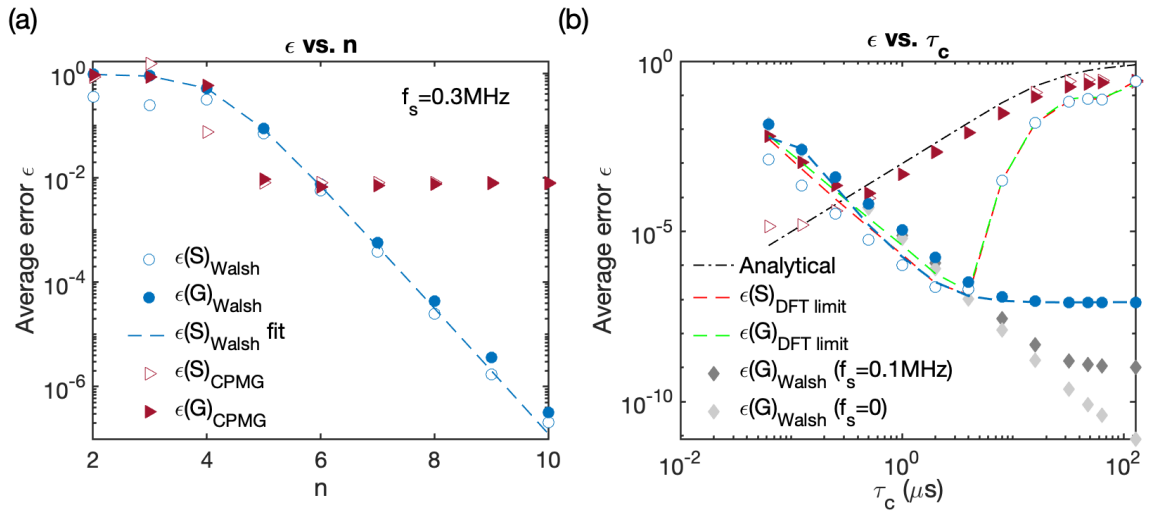

Figure 3-3: (a) n dependence of average reconstruction error. The OU noise parameters ω_s, b^2, τ_c and the sequence time T are the same as the inset (a) in Figure 3-2. (b) τ_c dependence of average reconstruction error. Parameters b^2 and T are same as (a). n is fixed as 10. Two Walsh cases with $\omega_s = 0$ and $\omega_s = (2\pi)0.1$ MHz are included as a comparison. The color rules are the same as (a) except for notifications. The analytical curve plots the $|\Delta\chi/\chi|^2$ in Equation (2.51). DFT-limited (Section 2.2.4) $\epsilon(S)$ and $\epsilon(G)$ are the errors of noise spectrum and arithmetic auto-correlation obtained respectively through DFT of discretized theoretical $G(t_j)$ and $S(\omega_j)$.

the reconstruction average errors by varying the number of sequences n, i.e. the reconstruction average errors as a function of n. The results are shown in the inset (a) of Figure 3-3. When n becomes larger, the reconstruction average error of the Walsh method keeps decreasing, while the reconstruction average error of the CPMG method decreases at a similar rate, and then decreases faster, and then saturates and reaches its plateau when $n = 6$. The inset (a) demonstrates that, for either the arithmetic auto-correlation $G(t)$ reconstruction or the noise spectrum $S(\omega)$ reconstruction, the Walsh method can conduct a more accurate reconstruction as the number of sequences n increases to a sufficient large one. However, the CPMG method can only provide more information in the higher frequency range but has minor effects in the low frequency range as n increases with more samplings. The advantages of the Walsh method become more prominent when the overall noise spectrum concentrates in a low frequency range.

In Ref. [82], it was known that the average error of the CPMG method is dom-

inated by the relation between the correlation time τ_c and the sequence time T. To validate the error of the Walsh method is not restricted by the relation, we analyze the variation of the reconstruction error as a function of the correlation time τ_c in the inset (b) of Figure 3-3 with $n = 10$ fixed. As we discussed in Section 2.2, the Walsh reconstruction method has two main types of errors:

- the error of arithmetic auto-correlation $G(t)$ reconstruction in time domain resulted from discretization error;
- the error of noise spectrum $S(\omega)$ reconstruction in frequency domain caused by DFT (Section 2.2.4).

To exclude the potential second error mentioned above, we firstly compare the average error of the arithmetic auto-correlation $G(t)$ reconstruction by using the Walsh method with the average error of the noise spectrum $S(\omega)$ reconstruction by using the CPMG method, which means we now only look into the $\epsilon(S)_{CPMG}$ related error data (hollow red triangles) and the $\epsilon(G)_{Walsh}$ related error data (solid blue dots) in Figure 3-3 (b). We then can conclude that the $\epsilon(S)_{CPMG}$ fits well the analytical error prediction line (the dark grey dashed line) [82], which increases as τ_c increases and finally reaches its plateau, while the $\epsilon(G)_{Walsh}$ performs in an opposite direction, which decreases as τ_c increases and saturates. Based on Equation (3.5), we can tell that, for an OU noise with non-zero ω_s, both ω_s and τ_c affect the reconstruction average error. For a simpler situation, when ω_s is zero, the correlation time, or rather, the decay time τ_c is the only factor that leads to the reconstruction average error theoretically and the error decreases as τ_c becomes larger. Similarly, when ω_s is non-zero but τ_c is small, τ_c can lead to the imperfect sampling of the decay feature, which dominates the average error. However, when ω_s is non-zero and τ_c is large, larger ω_s can result in the imperfect sampling of the oscillatory feature and also can contribute to a larger saturation error which can be concluded from the inset (b) of Figure 3-3 (dark and light grey dots). Therefore, the Walsh reconstruction method should be able to accurately reconstruct the arithmetic auto-correlation $G(t)$ with sufficient sampling in time domain.

After understanding the advantages the Walsh reconstruction method has in the time domain, we will analyze the error of noise spectrum $S(\omega)$ reconstruction by using the Walsh method, where the additional error caused by DFT should be taken into consideration. This additional error may come from two causes:

- finite range of time domain that does not capture the full decay feature governed by the noise correlation;
- finite sampling which does not capture the high frequency micro-motion.

In the inset (b) of Figure 3-3, we exclude the second possible cause by setting a very large N ($N = 2^{10}$ in our simulation) such that the limitation is only given by the first cause. Then, we plot the DFT of the theoretical $G(t_j)$ (the green dashed line), which dominates the noise spectrum reconstruction error $\epsilon(S)_{Walsh}$ when τ_c is large. Similarly, we plot the inverse DFT of the theoretical $S(\omega_j)$ (the red dashed line), which dominates the auto-correlation reconstruction error $\epsilon(G)_{CPMG}$ when τ_c is small due to the imperfect capture of high frequency component with finite frequency range. We note that with the knowledge of the noise model, these limitations can be overcome by fitting and extending the data to an infinite range before performing Fourier transform.

As a summary for the average reconstruction errors in terms of the comparison between the CPMG reconstruction method and the Walsh reconstruction method, we have results and conclusions included in Table 3.1.

3.3.2 Reconstruction comparison between the Carr-Purcell-Meiboom-Gill method and the Walsh method with the individual error

In addition to the overall performance of the noise reconstruction discussed in Section 3.3.1, in this Section, we discuss the error of individual points in the reconstructed spectrum or the reconstructed arithmetic auto-correlation. The metric to quantify the error of individual points has been defined as the Equation (3.9).

Table 3.1: Summary of the comparison between the Walsh reconstruction method and the CPMG reconstruction method.

Properties	CPMG reconstruction method	Walsh reconstruction method
Principle	frequency-space sampling with δ-like filter functions	time-space sampling, spectrum obtained by Fourier transform
Error source	δ-function approximation of the filter functions	(1) time-space sampling; (2) Fourier transform of finite time series (especially for $\tau_c \sim T$)
Error analysis	(1) $T \gg \tau_c$, almost perfect; (2) $T \sim \tau_c$, peak values bad, zero frequency bad	(1) peak values better than CPMG when $T \sim \tau_c$; (2) high frequency part is usually bad due to insufficient time-domain sampling
Improvement	$\chi \propto TS(\omega)$, measure the slope of $\chi \sim T$	(1) increase sampling; (2) properly increase T
Advantages	Easy and flexible to implement	(1) the arithmetic auto-correlation $G(t)$ reconstruction is (almost) perfect, only set by the sampling; (2) low frequency (near zero frequency) good performance; (3) peak values accuracy simply improved by increasing sampling
Disadvantages	the arithmetic auto-correlation $G(t)$ reconstruction is both affected by the accuracy of the reconstructed noise spectrum $S(\omega)$ and Fourier transform with finite time series	the noise spectrum $S(\omega)$ reconstruction is both affected by the accuracy of the reconstructed arithmetic auto-correlation $G(t)$, sampling and Fourier transform with finite time series

In Figure 3-4, we show an example of the spectrum reconstruction error, where the Walsh method has larger errors at larger frequencies due to insufficient time-space sampling. When the number of sequences n increases, the error for the Walsh reconstruction method decreases for the overall frequencies while the error for the CPMG reconstruction method decreases only for larger frequencies due to the effect of considering more higher harmonics for the high frequency components.

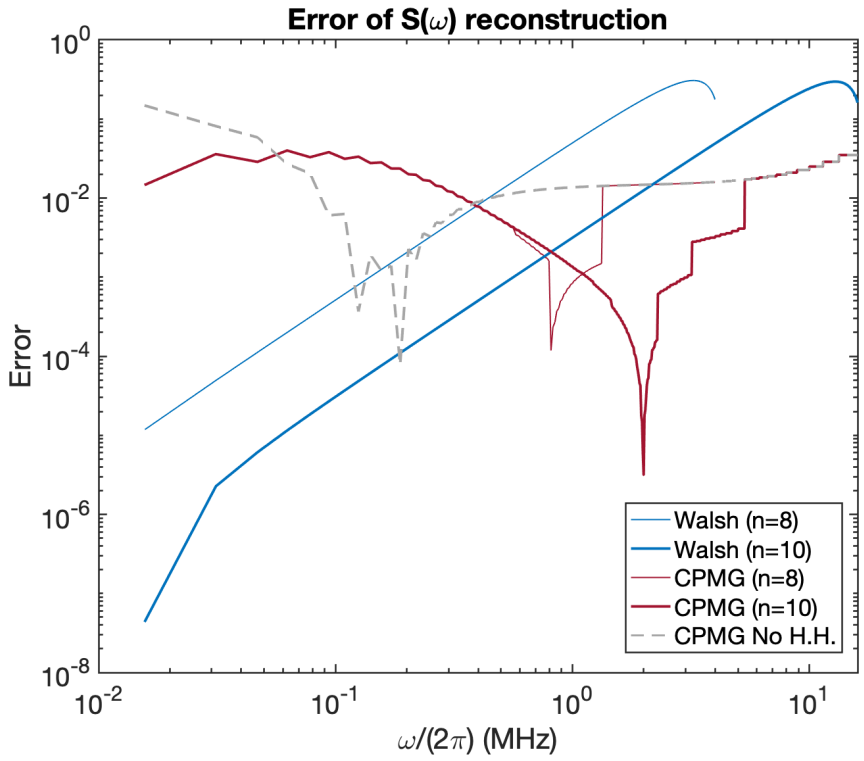

Figure 3-4: Errors of individual points in the reconstructed noise spectrum $S(\omega)$ by using the Walsh reconstruction method and the CPMG reconstruction method. The parameters related to the OU noise model we set here are $\omega_s = 0$, $\tau = 1$ μs, $b^2 = 0.003125$ μs.

3.4 Statistical analysis of the Ornstein-Uhlenbeck noise model

As we discussed in Section 3.3, in terms of the noise reconstruction comparison, we simulate the attenuation functions by directly calculating the integral in Equa-

tion (2.7). However, those simulations assume an infinite number of experimental averages or noise instances, which actually cannot be achieved in practical applications and cannot conduct a comprehensive evaluation on the possible errors induced by the stochastic nature of the noise. Therefore, we additionally dive into the statistical analysis of the OU noise model and draw conclusions about the potential effects of insufficient numbers of experiments for averaging or finite noise instances in this Section.

As shown in Section 3.1.1, we can use the Equation (3.1) defined in Ref. [36, 37] to generate a static OU noise following a stationary Gaussian distribution. By updating the time trace of the noise in the same fashion as the Equation (3.1), we can obtain the noise functions at the following time nodes written as:

$$\omega(t+2dt) = \omega(t+dt)e^{-\frac{dt}{\tau_c}} + r_1\sqrt{b^2(1-e^{-\frac{2dt}{\tau_c}})} \tag{3.13}$$

$$= \omega(t)e^{-2\frac{dt}{\tau_c}} + r_2\sqrt{b^2(1-e^{-\frac{2dt}{\tau_c}})}e^{-\frac{dt}{\tau_c}} + r_1\sqrt{b^2(1-e^{-\frac{2dt}{\tau_c}})} \tag{3.14}$$

$$\cdots \tag{3.15}$$

$$\omega(t+kdt) = \omega(t)e^{-k\frac{dt}{\tau_c}} + \left(r_1 + r_2e^{-\frac{dt}{\tau_c}} + \cdots + r_ke^{-(k-1)\frac{dt}{\tau_c}}\right)\sqrt{b^2(1-e^{-\frac{2dt}{\tau_c}})}, \tag{3.16}$$

where k is a positive integer and is used to present the time node after kdt since t.

Correspondingly, based on the Equation (3.3) defined in Section 3.1.1, the arithmetic auto-correlation $G(kdt)$ is then calculated as:

$$G(kdt) = \langle\omega(t+kdt)\omega(t)\rangle = b^2e^{-\frac{kdt}{\tau_c}}, \tag{3.17}$$

where we use the fact that a chi-squared distribution can be constructed by squaring a single standard normal distribution [47], which means that since $\omega(t)/b$ satisfying a standard normal distribution, i.e. $\omega(t)/b \sim N(0,1)$, $\omega(t)^2/b^2$ is effectively a chi-squared distribution, i.e. $\omega(t)^2/b^2 \sim \chi_1^2$. Note that when the noise trace is generated from an initial time t_0 with a constant value $\omega(t_0) = \text{const.}$, the correlation between times t and $t+kdt$ is $\langle\omega(t+kdt)\omega(t)\rangle = b^2e^{-\frac{kdt}{\tau_c}}(1-e^{-2\frac{t-t_0}{\tau_c}})$, which can be reduced to Equation (3.17) only when $t - t_0 \gg \tau_c$ [37]. In practical simulation, we can set

the initial point to a random number $\omega(0) = br_1$ satisfying a Gaussian distribution to avoid such a problem.

Since the Equation (3.17) is obtained under the assumption that sufficient numbers of averages have been applied, it is crucial to have an estimate of the number of averages required when it comes to practical implementations and applications. For a single measurement (or noise instance), the "arithmetic auto-correlation" based on the Equation (3.17) can be written as:

$$\omega(t+kdt)\omega(t) = \omega(t)^2 e^{-\frac{kdt}{\tau_c}} + \omega(t)(r_1 + r_2 e^{-\frac{dt}{\tau_c}} + \cdots + r_k e^{-(k-1)\frac{dt}{\tau_c}})\sqrt{b^2(1-e^{-\frac{2dt}{\tau_c}})} \tag{3.18}$$

$$= b^2 e^{-\frac{kdt}{\tau_c}} + \epsilon_0 + \epsilon_1, \tag{3.19}$$

where ϵ_0 and ϵ_1 both are zero-mean random variables corresponding to the first and second terms in the Equation (3.18). The variance of the summation $(\epsilon_0 + \epsilon_1)$ can be calculated through the following steps:

$$var(\epsilon_0) = 2b^4 e^{-\frac{2kdt}{\tau_c}}, \tag{3.20}$$

$$var(\epsilon_1) = b^4(1-e^{-\frac{2dt}{\tau_c}})(1 + e^{-\frac{2dt}{\tau_c}} + e^{-\frac{4dt}{\tau_c}} + \cdots + e^{-\frac{2(k-1)dt}{\tau_c}}) \tag{3.21}$$

$$= b^4(1-e^{-\frac{2dt}{\tau_c}})\frac{1-e^{-\frac{2kdt}{\tau_c}}}{1-e^{-\frac{2dt}{\tau_c}}} \tag{3.22}$$

$$= b^4(1-e^{-\frac{2kdt}{\tau_c}}), \tag{3.23}$$

$$cov(\epsilon_0, \epsilon_1) = 0, \tag{3.24}$$

$$var(\epsilon_0 + \epsilon_1) = var(\epsilon_0) + var(\epsilon_1) + cov(\epsilon_0, \epsilon_1) \tag{3.25}$$

$$= b^4(1 + e^{-\frac{2kdt}{\tau_c}}). \tag{3.26}$$

Therefore, if the number of averages is finite and denoted by $\langle\rangle_N$ where the subscript N represents the number of averages, the variance of the arithmetic auto-

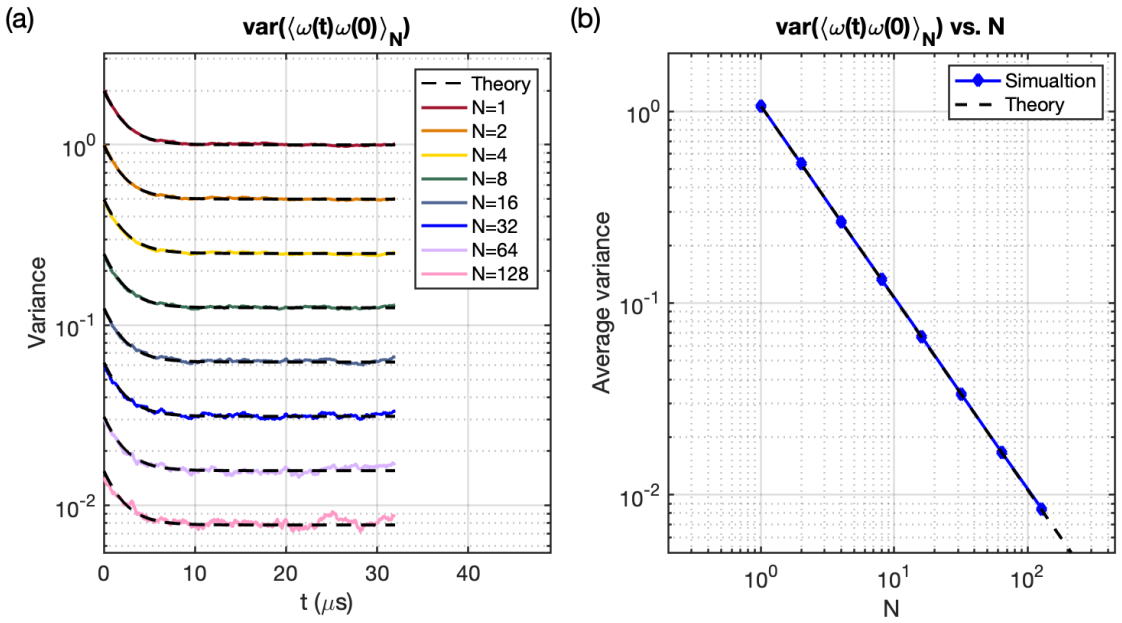

Figure 3-5: Variance of $\langle\omega(t)\omega(0)\rangle_N$ in a simulated OU noise when $\tau_c = 4$ μs, $b^2 = 1$ μs, $\omega_s = 0$ (Note that ω_s represents a nonzero frequency shift of the noise source and we have defined it earlier in Section 3.1.1). (a) Variance of $G(t)$ in a simulated static OU noise trace. We use a time step 0.03125 μs and simulate the noise from 0 to 32 μs with $2^{16} = 65536$ repetitions. Then, the simulated noise traces are correspondingly divided into 2^{16-n} groups with size $N = 2^n$ such that the variance of the mean value of different group size can be calculated. The theory curve is plotted using the function $\frac{b^4(1+e^{-2t/\tau_c})}{N}$. (b) The mean value of variances over all points in the time traces for each N in (a) plotted as a function of N.

correlation can be written as:

$$var(\langle\omega(t_1)\omega(t_2)\rangle_N) = \frac{b^4(1+e^{-\frac{2|t_1-t_2|}{\tau_c}})}{N}, \tag{3.27}$$

and the ratio of the standard deviation to the arithmetic auto-correlation is then derived as:

$$\frac{std(\langle\omega(t_1)\omega(t_2)\rangle_N)}{\langle\omega(t_1)\omega(t_2)\rangle} = \frac{(1+e^{\frac{2|t_1-t_2|}{\tau_c}})}{\sqrt{N}}, \tag{3.28}$$

which increases with the time difference. The relations derived above are validated numerically in Figure 3-5, where we simulate an OU noise and plot the simulated predicted variance of the arithmetic auto-correlation $\langle\omega(t)\omega(0)\rangle_N$ and the theoretical variance as well. For applications in practice, the Equations (3.27) and (3.28) can

be used to evaluate whether the number of averages is sufficient enough or not. In particular, when the number of averages is not adequate, the relative error in Walsh reconstruction method may be instead dominated by the fluctuations of the noise source itself especially for those points with larger t in the arithmetic auto-correlation $G(t)$.

The analysis above only sets a theoretical upper bound without a precise value to elaborate the error in the arithmetic auto-correlation reconstruction with the Walsh method. The discretization of the continuous arithmetic auto-correlation takes the average value of $\omega(t_j)\omega(t_k)$ (i.e. $\langle\omega(t_j)\omega(t_k)\rangle$) where $t_j \in [(j-1)T/N, jT/N], t_k \in [(k-1)T/N, kT/N]$ as the $G_N(j-k)$, which achieves an average effect and partly decreases the influence of insufficient averages. In addition, under the stationary noise assumption, the arithmetic auto-correlation is only dependent on the time difference, so its reconstruction is an effective "average" of many "time pairs" in the time trace with the same time difference, which yields less reconstruction errors as well. We note that although these effects could potentially allow less averages for a satisfying reconstruction, in Walsh experiments the minimal inter-pulse delay is usually set to be smaller than the noise correlation time (for satisfying sampling in time dimension), and the improvement of either aforementioned "average" effect is minor due to the strong correlation within each inter-pulse delay.

Chapter 4

Experimental demonstration of Walsh noise spectroscopy with a single nitrogen-vacancy center in diamond

Noise spectroscopy [66, 79], as a tool to characterize the noise within a quantum system coupled with the external environment, plays an important role in quantum technology and quantum engineering.

In practice, recently dynamical decoupling methods such as CPMG method and XY method have been widely used to demonstrate various characterizations of noise spectrum in terms of inclusive quantum sensors including solid state spins systems such as quantum dots [63, 29] and nitrogen-vacancy (NV) centers in diamond [78, 9], superconducting circuits such as superconducting flux qubit [18], et al. In our work, to conduct noise reconstruction experimentally, we use a single nitrogen-vacancy (NV) center in diamond as a quantum sensor.

In Section 4.1, we briefly introduce what is the NV center in diamond by showing its crystal structure and its energy levels respectively, which can help understand why a single NV center in diamond can be used as a quantum sensor in experiment. Next, in Section 4.2, we will show the proof-of-principle demonstration of experimental results. More specifically, in Section 4.2.1, we introduce the experimental setup used for experiments such as multi-π pulse sequence generation et al. In Section 4.2.2,

we firstly recall the main conclusions we have drawn from Section 3.3.1 in terms of the reconstruction comparison between the CPMG method and the Walsh method in simulation. Then based on the experimental results, we will compare the simulation conclusions with the experimental results and finally discuss several main potential errors induced in experiment by using the Walsh reconstruction method and a few corresponding potential ways to improve its experimental performance.

4.1 Nitrogen-vacancy centers in diamond

The NV center is a point defect in diamond and it is stable in the diamond crystal structure [46, 31]. It consists of a nearest-neighbor pair of a nitrogen atom that substitutes in place of a carbon atom and a vacancy on an adjacent lattice site, resulting in one of the defect's symmetry axes being along four possible orientations, shown in Figure 4-1 (a) [6, 81]. Analogous to energy level structures used in atomic physics, the NV center has a triplet ground state, a triplet excited state and several meta-stable states [30]. As shown in Figure 4-1 (b), the ground triplet state corresponding to $|m_s = 0\rangle$ and $|m_s = \pm 1\rangle$ has a zero-field splitting $D \approx 2.87GHz$ [68]. The $|m_s = \pm 1\rangle$ states have an additional splitting proportional to an external magnetic field parallel along the NV symmetry axis.

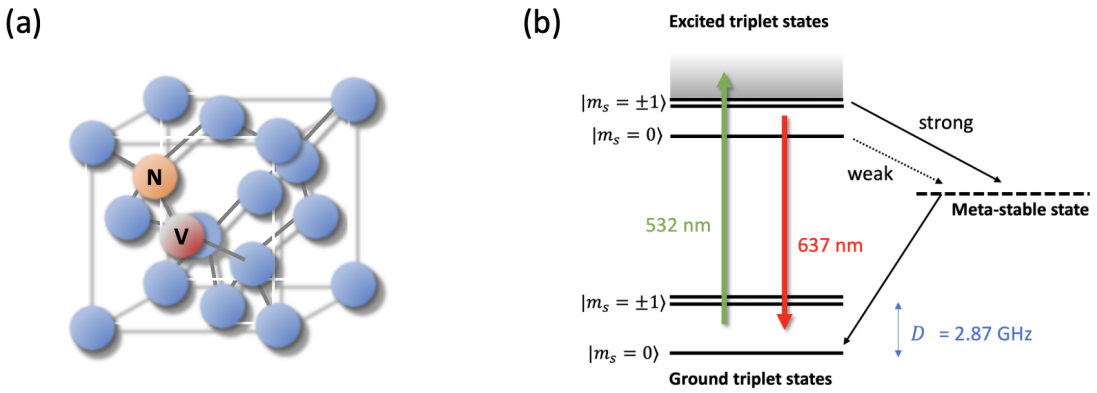

Figure 4-1: NV center in diamond. (a) The structure of a NV center. (b) Energy levels of the NV center.

The atom-like properties of NV centers can help in its initialization and read-

out [40]. The NV center can be excited from its ground state to its excited state by a green laser ($\lambda \approx 532nm$) [68] and decay through the metastable singlet state back to its ground state. The process is similar to the readout for the spin population in $|m_s = 0\rangle$ which is achieved by observing the intensity of the red fluorescence ($\lambda \approx 637nm$) [68] while illuminating the system with a green laser. Then, the population will concentrate into the $|m_s = 0\rangle$ state after the excitation and spontaneous decay. By applying a microwave whose frequency is on resonance with the energy difference between $|m_s = 0\rangle$ and $|m_s = 1\rangle$ (or between $|m_s = 0\rangle$ and $|m_s = -1\rangle$), we can create a superposition state between the corresponding two states, in a manner that we could use a method for a two-level system to analyze the process. Subsequently, we can control the coherent spin qubit to measure external physical quantities such as external magnetic [86, 62, 8, 30] and electric [32] fields and time dependent noise.

4.2 Comparison of noise reconstruction

In this section, we will firstly introduce the experiment setup we use in the laboratory and secondly demonstrate experimental results, and finally discuss the experimental performance and corresponding improvements we can conduct in practice.

4.2.1 Experimental setup

We use a homemade confocal optical setup [93, 57], where the 532 nm laser (SPROUT, Lighthouse Photonics) is applied to prepare a spin qubit to its initial state, and the red fluorescence is collected by a single photon detector (Perkin Elmer SPCM-AQRH-14). We use a permanent magnet to generate a static magnetic field at around 460 G (i.e. 0.046 T) along one of the NV axes to lift the degeneracy of the NV ground states. In practice, two states $|m_S = 0\rangle$ and $|m_S = -1\rangle$ of the NV center are used as a spin qubit. The 1.5 GHz microwave signal is generated by a RF signal generator (Stanford Research System). The phase-controlled 50 MHz microwave signal is firstly generated by an arbitrary waveform generator (WX1284C) and secondly amplified by an amplifier (Mini-Circuits, ZHL-30W-252-S+) and then applied to the diamond by

a 25 μm diameter straight copper wire, which delivers the microwave (MW) control fields to apply pulse sequences. These two microwave signals are mixed by an IQ mixer. All these electronic and optical devices/instruments are synchronized by a pulse blaster (PulseBlasterESR-PRO 500).

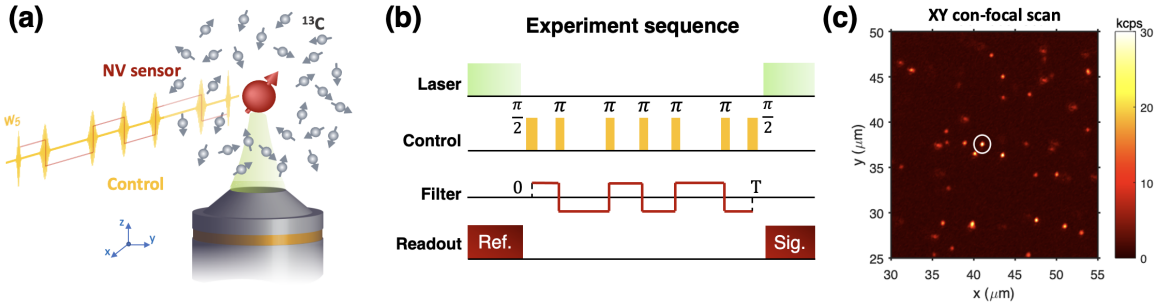

Figure 4-2: Experimental setup. (a) A single NV in diamond surrounded by a spin bath of ^{13}C. (b) An example experiment sequence for the sixth Walsh sequence. (c) XY con-focal scan to position a single NV center. The NV center we use at the depth around 30 μm of the diamond sample is highlighted by the white circle.

We use this setup to reconstruct noise spectrum with a specific quantum sensor - a single NV center in diamond. As is shown in the inset (a) of Figure 4-2, at the depth around 30 μm of the diamond sample, ^{13}C nuclear spins are the main composition of the spin bath. The inset (b) of Figure 4-2 demonstrates an example sequence we use in experiment, where the sixth Walsh sequence is applied. The inset (c) of Figure 4-2 shows how we position a single NV center through XY con-focal scan.

4.2.2 Experimental results and performance discussion

Before showing the experimental results, we first briefly recall the simulation results and conclusions.

For the Walsh reconstruction method, we have:

- The arithmetic auto-correlation $G(t)$ is well reconstructed before the noise spectrum $S(\omega)$. The error of the arithmetic auto-correlation $G(t)$ is sourced from the relation between the time-space sampling T/N and the characteristic noise properties.

For an OU noise with a frequency shift ω_s, the characteristic timescale is given by the correlation time τ_c and the noise period $T_s = 2\pi/\omega_s$.

- The noise spectrum $S(\omega)$ is reconstructed through DFT of the arithmetic auto-correlation $G(t)$. In addition to the error that linearly propagated from the arithmetic auto-correlation $G(t)$, DFT of finite time series introduces the error dominated by the relation between τ_c and T.

For the CPMG reconstruction method, we have:

- The noise spectrum $S(\omega)$ is reconstructed before the arithmetic auto-correlation $G(t)$ and the error is dominated by the relation between the frequency-space sampling π/T and the characteristic spectrum properties including noise frequencies and linewidths. The main error is sourced from the δ-function approximation of the filter functions, which can be eliminated when $\tau_c/T \ll 1$.

- $G(t)$ is reconstructed through DFT of $S(\omega)$. In addition the error that linearly propagated from $S(\omega)$, DFT of finite time series introduces error dominated by the relation between π/T and the characteristic spectrum properties including the noise frequency shift ω_s, linewidths $\sim 1/\tau_c$, as well as the frequency-sampling range.

Proof-of-principle demonstration of experimental results

We reconstruct the arithmetic auto-correlation $G(t)$ and the noise spectrum $S(\omega)$ by applying the CPMG sequences and the Walsh sequences respectively in the experimental setup demonstrated in Section 4.2.1. The sequence parameters we set in experiment include that the sequence time is $T = 8$ μs, the number of sequences is $N = 2^5 = 32$. As is shown in the panel (a) of Figure 4-3, both the Walsh method and the CPMG method can reconstruct the arithmetic auto-correlation $G(t)$ with an oscillation frequency around 0.5 MHz. Correspondingly, we can consistently conclude that in the panel (b) of Figure 4-3, both methods can reconstruct the noise spectrum with a peak around 0.5 MHz, which matches the the predicted Larmor frequency of

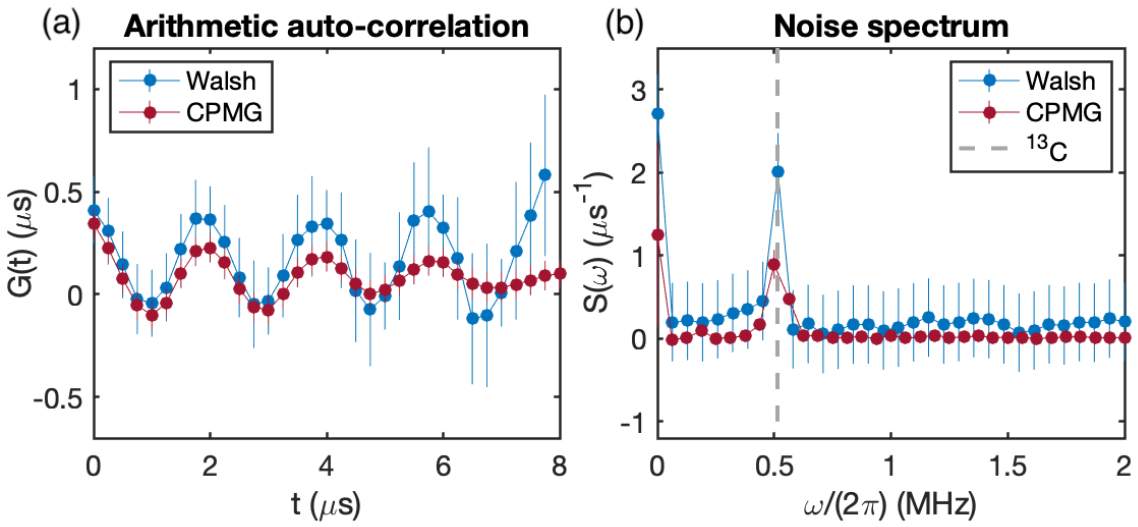

Figure 4-3: Experimental results. (a) Reconstructed arithmetic auto-correlation $G(t)$. (b) Reconstructed noise spectrum $S(\omega)$. The same sequence time $T = 8$ μs and number of sequences $N = 2^5 = 32$ are used in (a) and (b).

the nuclear spin ^{13}C considering ^{13}C nuclear spins are the main composition of the spin bath (Figure 4-2 (a)).

Performance discussion

In Section 3.3 (Figures 3-2 and 3-3), we conclude via simulation that the Walsh method can (almost) perfectly reconstruct the arithmetic auto-correlation $G(t)$ and can improve the reconstructed noise spectrum $S(\omega)$ by simply increasing its time-space sampling, which indicates that the Walsh method can outperform the CPMG reconstruction method with finite time series and a relatively large pulse number. However, as is shown in Figure 4-3, the error bar of the reconstructed arithmetic auto-correlation $G(t)$ and noise spectrum $S(\omega)$ by using the Walsh method is larger than that by using the CPMG method. In addition, as time t increases, the error bar becomes larger for the Walsh method. These indicate that due to the existence of other practical errors, the alignment between experimental results and the simulation results may vary conditional on different scenarios with different parameters.

In the remaining part of Section 4.2.2, we will look into and analyze several main factors that induced in experiment, from which some potential improvements we can

conduct will be enlightened.

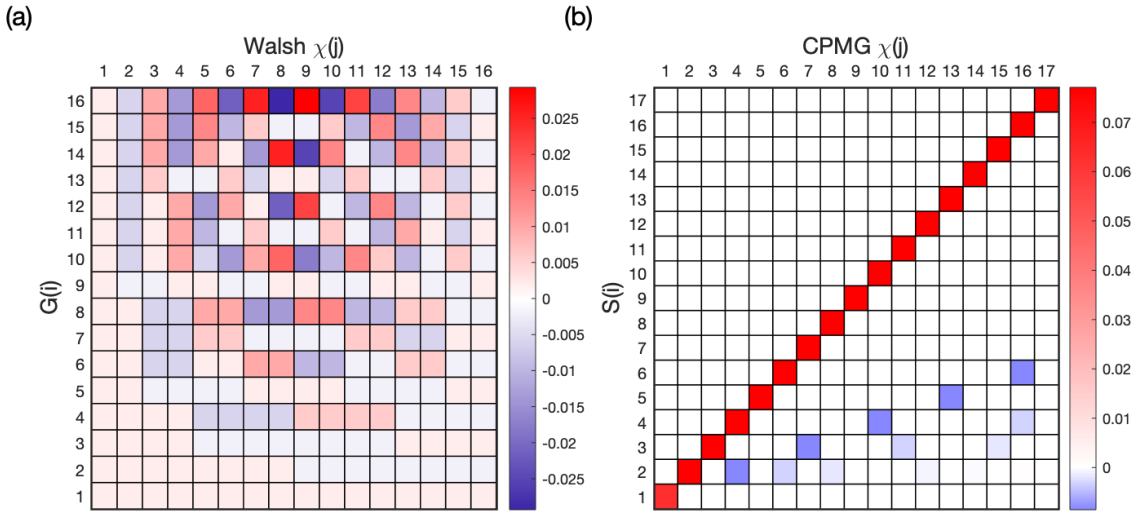

Figure 4-4: Error propagation. (a) The transform matrix from $\chi(j)$ to $G(i)$ when using the Walsh reconstruction method. (b) The transform matrix from $\chi(j)$ to $S(i)$ when using the CPMG reconstruction method. The same parameters $T = 32$ and $N = 2^4 = 16$ are used in (a) and (b).

Firstly, during the data collection, the error will be introduced. The relative error of the attenuation χ (i.e. $\frac{\sigma_\chi}{\chi}$) can be written as:

$$\frac{\sigma_\chi}{\chi} = \frac{2\sigma_P \cdot e^\chi}{c \cdot \chi}, \tag{4.1}$$

where c is the signal contrast and σ_P is the uncertainty of the projective measurement, which can be caused by photon shot-noise limit or projection limit [11]. Based on the definition of Eq. (4.1), the minimal value of the relative error $\frac{\sigma_\chi}{\chi}$ can be reached when the value of the attenuation χ is 1 and the uncertainty of the projective measurement σ_P is independent of the attenuation χ [11]. Consequently, when either the value of the attenuation χ increases or decreases, the relative error $\frac{\sigma_\chi}{\chi}$ will increase. As we discussed in Chapter 2, the Walsh reconstruction method relies on a series of pulse sequences while the typical dynamical decoupling methods used in noise spectroscopy such as the CPMG reconstruction method only simply relies on a single pulse sequence. Therefore, for the Walsh method, different sequence components have different decoherence. For example, in Figure 3-1 (a), the w_1 sequence is

actually a Ramsey, which naturally has a much faster decoherence compared to the remaining $w_2, w_3, \ldots, w_{16}$ sequences. Furthermore, since the Walsh reconstruction method involves three linear transforms when the attenuation χ is being transformed to the noise spectrum $S(\omega)$, the errors of the attenuation χ generated even only in a few sequences, particularly in the first Ramsey sequence, are propagated from the attenuation χ to the arithmetic auto-correlation $G(t)$ by using two non-diagonal matrices (Section 2.2) and contaminate most points in the reconstructed arithmetic auto-correlation $G(t)$; and then the errors spreading in the the arithmetic auto-correlation $G(t)$ are further propagated to the noise spectrum $S(\omega)$. On the other hand, for the CPMG reconstruction method, the transformation from the attenuation χ to the noise spectrum $S(\omega)$ is almost diagonal. The comparison of the transformations for the Walsh method and the CPMG method with same parameter profile is explicitly and respectively. shown in Figure 4-4 (a) and (b). The panel (a) is the transform matrix used in the Walsh method transforming the discrete attenuation $\chi(j)$ through a complicated non-diagonal matrix to the discrete arithmetic auto-correlation $G(i)$. The panel (b) is the transform matrix used in the CPMG method transforming the discrete attenuation $\chi(j)$ through a close-to-diagonal matrix to the discrete noise spectrum $S(i)$ even after we take the higher order harmonics into consideration. This error propagation effect in the Walsh method largely limits its performance in noise spectroscopy in practice. One direct way to eliminate this limitation is to apply a sequence consisting of M concatenated Walsh sequence blocks and to measure the decoherence as a function of M. Then we can obtain a more precise value of the attenuation χ [83, 82] after correspondingly fitting the results to an exponential function of M.

Another error source can be the statistical averaging over sufficient realizations of the noise process. When we discuss the Walsh reconstruction method in Section 2.2, both of the auto-correlations (the arithmetic and the logical ones) are well defined in Equation (2.55) and Equation (2.58) conditional on sufficient average of noise instances such that:

$$\langle \omega(t)\omega(0) \rangle = G(t) + \epsilon(t) \approx G(t). \tag{4.2}$$

However, when the average number of noise instances is large enough, we cannot neglect the $\epsilon(t)$ term in Equation (4.2), and consequently cannot neglect the error induced by the $\epsilon(t)$ term. For an OU process, as time t increases, the relative variance of the arithmetic auto-correlation $G(t)$ increases in an exponential-like trend due to the exponential decrease of its average value, which will lead to a larger relative error of the reconstructed arithmetic auto-correlation $G(t)$ when t becomes larger (the panel (a) of Figure 4-3). Although the time discretization and the matrix transformations during the Walsh reconstruction method can partially offset these effects, one direct way to suppress the upper bound of the induced error is to increase the average number in experiment.

Chapter 5

Conclusion and outlook

In this thesis, we proposed and demonstrated a digital noise reconstruction method called the Walsh method based on Walsh dynamical decoupling sequences. Our method is intrinsically compatible with time discretization and the sequence control in dynamical decoupling based experiments.

In Chapter 2, we introduce (i) several typical dynamical decoupling methods with a focus on the dynamical decoupling-based noise reconstruction method - the CMPG method; (ii) the Walsh reconstruction method in theory.

In Chapter 3, we compare the Walsh reconstruction method and the CPMG reconstruction method by performing numerical simulation. From the simulation results, we conclude that our Walsh method can (almost) perfectly reconstruct the arithmetic auto-correlation and its performance can be easily improved under limited sequence time by increasing the time-space sampling.

In Chapter 4, we show proof-of-principle experiments to characterize the environmental noise of a single NV center in diamond with ^{13}C nuclear spins as the main composition of the spin bath. In addition, we discuss the potential sources of experimental errors during the method practical implementation and propose potential improvements.

One direction of interest for future research based on the work mentioned in this thesis is to extend the noise reconstruction to quantum-classical models, where both the quantum and classical part of a noise bath can be reconstructed by the Walsh

method efficiently [43, 72, 85, 49, 22]. Another direction of interest to explore but out of the scope of the work is to study the dynamics of a quantum system under Walsh sequences subjected to a non-classical or non-Gaussian noise [83, 64, 10, 24, 67], where novel phenomena such as anomalous decoherence [44, 99] were discovered. Also, it will be an interesting topic to apply Walsh sequences to reconstruct the polyspectra of a non-Gaussian noise [64], or to perform cross-spectroscopy using multiple qubits [52, 66, 84]. In addition, unlike periodic-dynamical decoupling-based noise reconstruction methods where different pulse patterns contribute to the performance improvement [43, 70, 58], the optimal control in Walsh noise reconstruction is a non-trivial task due to the asymmetric pulse patterns [71], but is important for its practical use.

Bibliography

[1] V Agrawal, P Neuzil, and DW Van der Weide. A microfabricated tip for simultaneous acquisition of sample topography and high-frequency magnetic field. *Applied Physics Letters*, 71(16):2343–2345, 1997.

[2] Mustafa Ahmed Ali Ahmed, Gonzalo A Alvarez, and Dieter Suter. Robustness of dynamical decoupling sequences. *Physical Review A*, 87(4):042309, 2013.

[3] Yacine Aït-Sahalia. Maximum likelihood estimation of discretely sampled diffusions: a closed-form approximation approach. *Econometrica*, 70(1):223–262, 2002.

[4] Gonzalo A Alvarez, Ashok Ajoy, Xinhua Peng, and Dieter Suter. Performance comparison of dynamical decoupling sequences for a qubit in a rapidly fluctuating spin bath. *Physical Review A*, 82(4):042306, 2010.

[5] Gonzalo A Álvarez and Dieter Suter. Measuring the spectrum of colored noise by dynamical decoupling. *Physical Review Letters*, 107(23):230501, 2011.

[6] Silvia Arroyo-Camejo, Andrii Lazariev, Stefan W Hell, and Gopalakrishnan Balasubramanian. Room temperature high-fidelity holonomic single-qubit gate on a solid-state spin. *Nature Communications*, 5(1):1–5, 2014.

[7] Dave Morris Bacon. *Decoherence, control, and symmetry in quantum computers*. University of California, Berkeley, 2001.

[8] Gopalakrishnan Balasubramanian, IY Chan, Roman Kolesov, Mohannad Al-Hmoud, Julia Tisler, Chang Shin, Changdong Kim, Aleksander Wojcik, Philip R Hemmer, Anke Krueger, et al. Nanoscale imaging magnetometry with diamond spins under ambient conditions. *Nature*, 455(7213):648–651, 2008.

[9] Nir Bar-Gill, Linh My Pham, Chinmay Belthangady, David Le Sage, Paola Cappellaro, JR Maze, Mikhail D Lukin, Amir Yacoby, and Ronald Walsworth. Suppression of spin-bath dynamics for improved coherence of multi-spin-qubit systems. *Nature Communications*, 3(1):1–6, 2012.

[10] Edwin Barnes, Mark S Rudner, Frederico Martins, Filip K Malinowski, Charles M Marcus, and Ferdinand Kuemmeth. Filter function formalism beyond pure dephasing and non-markovian noise in singlet-triplet qubits. *Physical Review B*, 93(12):121407, 2016.

[11] John F Barry, Jennifer M Schloss, Erik Bauch, Matthew J Turner, Connor A Hart, Linh M Pham, and Ronald L Walsworth. Sensitivity optimization for nv-diamond magnetometry. *Reviews of Modern Physics*, 92(1):015004, 2020.

[12] Enrico Bibbona, Gianna Panfilo, and Patrizia Tavella. The ornstein–uhlenbeck process as a model of a low pass filtered white noise. *Metrologia*, 45(6):S117, 2008.

[13] MJ Biercuk, AC Doherty, and H Uys. Dynamical decoupling sequence construction as a filter-design problem. *Journal of Physics B: Atomic, Molecular and Optical Physics*, 44(15):154002, 2011.

[14] RC Black, FC Wellstood, E Dantsker, AH Miklich, D Koelle, F Ludwig, and J Clarke. Imaging radio-frequency fields using a scanning squid microscope. *Applied Physics Letters*, 66(10):1267–1269, 1995.

[15] Pascal Böhi, Max F Riedel, Theodor W Hänsch, and Philipp Treutlein. Imaging of microwave fields using ultracold atoms. *Applied Physics Letters*, 97(5):051101, 2010.

[16] Ajay Kumar Boyat and Brijendra Kumar Joshi. A review paper: noise models in digital image processing. *arXiv preprint arXiv:1505.03489*, 2015.

[17] Steven T Bramwell and Bernhard Keimer. Neutron scattering from quantum condensed matter. *Nature Materials*, 13(8):763–767, 2014.

[18] Jonas Bylander, Simon Gustavsson, Fei Yan, Fumiki Yoshihara, Khalil Harrabi, George Fitch, David G Cory, Yasunobu Nakamura, Jaw-Shen Tsai, and William D Oliver. Noise spectroscopy through dynamical decoupling with a superconducting flux qubit. *Nature Physics*, 7(7):565–570, 2011.

[19] Paola Cappellaro. *Lecture Notes*. MIT Course 22.51 Quantum Technology and Devices, 2020.

[20] Herman Y Carr and Edward M Purcell. Effects of diffusion on free precession in nuclear magnetic resonance experiments. *Physical Review*, 94(3):630, 1954.

[21] Kalok C Chan, G Andrew Karolyi, Francis A Longstaff, and Anthony B Sanders. An empirical comparison of alternative models of the short-term interest rate. *The Journal of Finance*, 47(3):1209–1227, 1992.

[22] L Childress, MV Gurudev Dutt, JM Taylor, AS Zibrov, F Jelezko, J Wrachtrup, PR Hemmer, and MD Lukin. Coherent dynamics of coupled electron and nuclear spin qubits in diamond. *Science*, 314(5797):281–285, 2006.

[23] Alexandre Cooper, Easwar Magesan, HoNam Yum, and Paola Cappellaro. Time-resolved magnetic sensing with electronic spins in diamond. *Nature Communications*, 5(1):1–7, 2014.

[24] Łukasz Cywiński. Dynamical-decoupling noise spectroscopy at an optimal working point of a qubit. *Physical Review A*, 90(4):042307, 2014.

[25] Łukasz Cywiński, Roman M Lutchyn, Cody P Nave, and S Das Sarma. How to enhance dephasing time in superconducting qubits. *Physical Review B*, 77(17):174509, 2008.

[26] G De Lange, ZH Wang, D Riste, VV Dobrovitski, and R Hanson. Universal dynamical decoupling of a single solid-state spin from a spin bath. *Science*, 330(6000):60–63, 2010.

[27] Ger de Lange, D Ristè, VV Dobrovitski, and R Hanson. Single-spin magnetometry with multipulse sensing sequences. *Physical Review Letters*, 106(8):080802, 2011.

[28] Christian L Degen, F Reinhard, and Paola Cappellaro. Quantum sensing. *Reviews of Modern Physics*, 89(3):035002, 2017.

[29] OE Dial, Michael Dean Shulman, Shannon Pasca Harvey, H Bluhm, V Umansky, and Amir Yacoby. Charge noise spectroscopy using coherent exchange oscillations in a singlet-triplet qubit. *Physical Review Letters*, 110(14):146804, 2013.

[30] Marcus W Doherty, Neil B Manson, Paul Delaney, Fedor Jelezko, Jörg Wrachtrup, and Lloyd CL Hollenberg. The nitrogen-vacancy colour centre in diamond. *Physics Reports*, 528(1):1–45, 2013.

[31] MW Doherty, F Dolde, H Fedder, Fedor Jelezko, J Wrachtrup, NB Manson, and LCL Hollenberg. Theory of the ground-state spin of the nv- center in diamond. *Physical Review B*, 85(20):205203, 2012.

[32] Florian Dolde, Helmut Fedder, Marcus W Doherty, Tobias Nöbauer, Florian Rempp, Gopalakrishnan Balasubramanian, Thomas Wolf, Friedemann Reinhard, Lloyd CL Hollenberg, Fedor Jelezko, et al. Electric-field sensing using single diamond spins. *Nature Physics*, 7(6):459–463, 2011.

[33] Joseph L Doob. The brownian movement and stochastic equations. *Annals of Mathematics*, pages 351–369, 1942.

[34] Demitry Farfurnik, Andrey Jarmola, Linh M Pham, Zhi-Hui Wang, Viatcheslav V Dobrovitski, Ronald L Walsworth, Dmitry Budker, and Nir Bar-Gill. Optimizing a dynamical decoupling protocol for solid-state electronic spin ensembles in diamond. *Physical Review B*, 92(6):060301, 2015.

[35] Hans Fischer. *A history of the central limit theorem: From classical to modern probability theory*. Springer Science & Business Media, 2010.

[36] Daniel T Gillespie. Exact numerical simulation of the ornstein-uhlenbeck process and its integral. *Physical Review E*, 54(2):2084, 1996.

[37] Daniel T Gillespie. The mathematics of brownian motion and johnson noise. *American Journal of Physics*, 64(3):225–240, 1996.

[38] Terry Gullion, David B Baker, and Mark S Conradi. New, compensated carr-purcell sequences. *Journal of Magnetic Resonance (1969)*, 89(3):479–484, 1990.

[39] Erwin L Hahn. Spin echoes. *Physical Review*, 80(4):580, 1950.

[40] R Hanson, FM Mendoza, RJ Epstein, and DD Awschalom. Polarization and readout of coupled single spins in diamond. *Physical Review Letters*, 97(8):087601, 2006.

[41] David Hayes, Kaveh Khodjasteh, Lorenza Viola, and Michael J Biercuk. Reducing sequencing complexity in dynamical quantum error suppression by walsh modulation. *Physical Review A*, 84(6):062323, 2011.

[42] Carl W Helstrom. Quantum detection and estimation theory. *Journal of Statistical Physics*, 1(2):231–252, 1969.

[43] Santiago Hernández-Gómez, Francesco Poggiali, Paola Cappellaro, and Nicole Fabbri. Noise spectroscopy of a quantum-classical environment with a diamond qubit. *Physical Review B*, 98(21):214307, 2018.

[44] Pu Huang, Xi Kong, Nan Zhao, Fazhan Shi, Pengfei Wang, Xing Rong, Ren-Bao Liu, and Jiangfeng Du. Observation of an anomalous decoherence effect in a quantum bath at room temperature. *Nature Communications*, 2(1):1–7, 2011.

[45] Gene Hunt. The relative importance of directional change, random walks, and stasis in the evolution of fossil lineages. *Proceedings of the National Academy of Sciences*, 104(47):18404–18408, 2007.

[46] F Jelezko, I Popa, A Gruber, C Tietz, J Wrachtrup, A Nizovtsev, and S Kilin. Single spin states in a defect center resolved by optical spectroscopy. *Applied Physics Letters*, 81(12):2160–2162, 2002.

[47] NL Johnson, S Kotz, and N Balakrishnan. Chi-squared distributions including chi and rayleigh. *Continuous Univariate Distributions*, 1:415–493, 1994.

[48] Kaveh Khodjasteh and Daniel A Lidar. Fault-tolerant quantum dynamical decoupling. *Physical Review Letters*, 95(18):180501, 2005.

[49] Shimon Kolkowitz, Quirin P Unterreithmeier, Steven D Bennett, and Mikhail D Lukin. Sensing distant nuclear spins with a single electron spin. *Physical Review Letters*, 109(13):137601, 2012.

[50] TW Kornack, RK Ghosh, and Michael V Romalis. Nuclear spin gyroscope based on an atomic comagnetometer. *Physical Review Letters*, 95(23):230801, 2005.

[51] Shlomi Kotler, Nitzan Akerman, Yinnon Glickman, Anna Keselman, and Roee Ozeri. Single-ion quantum lock-in amplifier. *Nature*, 473(7345):61–65, 2011.

[52] Damian Kwiatkowski and Łukasz Cywiński. Decoherence of two entangled spin qubits coupled to an interacting sparse nuclear spin bath: Application to nitrogen vacancy centers. *Physical Review B*, 98(15):155202, 2018.

[53] JE Lang, T Madhavan, J-P Tetienne, DA Broadway, LT Hall, Tokuyuki Teraji, TS Monteiro, Alastair Stacey, and LCL Hollenberg. Nonvanishing effect of detuning errors in dynamical-decoupling-based quantum sensing experiments. *Physical Review A*, 99(1):012110, 2019.

[54] Hwang Lee, Pieter Kok, and Jonathan P Dowling. A quantum rosetta stone for interferometry. *Journal of Modern Optics*, 49(14-15):2325–2338, 2002.

[55] Sheng-Chiang Lee, CP Vlahacos, BJ Feenstra, Andrew Schwartz, DE Steinhauer, FC Wellstood, and Steven M Anlage. Magnetic permeability imaging of metals with a scanning near-field microwave microscope. *Applied Physics Letters*, 77(26):4404–4406, 2000.

[56] Tim Leung and Xin Li. Optimal mean reversion trading with transaction costs and stop-loss exit. *International Journal of Theoretical and Applied Finance*, 18(03):1550020, 2015.

[57] Yi-Xiang Liu, Ashok Ajoy, Paola Cappellaro, et al. Nanoscale vector dc magnetometry via ancilla-assisted frequency up-conversion. *Physical Review Letters*, 122(10):100501, 2019.

[58] Michael Loretz, JM Boss, Tobias Rosskopf, HJ Mamin, D Rugar, and Christian L Degen. Spurious harmonic response of multipulse quantum sensing sequences. *Physical Review X*, 5(2):021009, 2015.

[59] Easwar Magesan, Alexandre Cooper, Honam Yum, and Paola Cappellaro. Reconstructing the profile of time-varying magnetic fields with quantum sensors. *Physical Review A*, 88(3):032107, 2013.

[60] Emilia P Martins. Estimating the rate of phenotypic evolution from comparative data. *The American Naturalist*, 144(2):193–209, 1994.

[61] AA Maudsley. Modified carr-purcell-meiboom-gill sequence for nmr fourier imaging applications. *Journal of Magnetic Resonance (1969)*, 69(3):488–491, 1986.

[62] Jeronimo R Maze, Paul L Stanwix, James S Hodges, Seungpyo Hong, Jacob M Taylor, Paola Cappellaro, Liang Jiang, MV Dutt, Emre Togan, AS Zibrov, et al. Nanoscale magnetic sensing with an individual electronic spin in diamond. *Nature*, 455(7213):644–647, 2008.

[63] J Medford, C Barthel, CM Marcus, MP Hanson, AC Gossard, et al. Scaling of dynamical decoupling for spin qubits. *Physical Review Letters*, 108(8):086802, 2012.

[64] Leigh M Norris, Gerardo A Paz-Silva, and Lorenza Viola. Qubit noise spectroscopy for non-gaussian dephasing environments. *Physical Review Letters*, 116(15):150503, 2016.

[65] Caspar F Ockeloen, Roman Schmied, Max F Riedel, and Philipp Treutlein. Quantum metrology with a scanning probe atom interferometer. *Physical Review Letters*, 111(14):143001, 2013.

[66] Gerardo A Paz-Silva, Leigh M Norris, and Lorenza Viola. Multiqubit spectroscopy of gaussian quantum noise. *Physical Review A*, 95(2):022121, 2017.

[67] Gerardo A Paz-Silva and Lorenza Viola. General transfer-function approach to noise filtering in open-loop quantum control. *Physical Review Letters*, 113(25):250501, 2014.

[68] Linh My Pham. *Magnetic field sensing with nitrogen-vacancy color centers in diamond*. Harvard University, 2013.

[69] Linh My Pham, Nir Bar-Gill, Chinmay Belthangady, David Le Sage, Paola Cappellaro, Mikhail D Lukin, Amir Yacoby, and Ronald L Walsworth. Enhanced solid-state multispin metrology using dynamical decoupling. *Physical Review B*, 86(4):045214, 2012.

[70] F Poggiali, P Cappellaro, and N Fabbri. Optimal control for one-qubit quantum sensing. *Physical Review X*, 8(2):021059, 2018.

[71] Haoyu Qi, Jonathan P Dowling, and Lorenza Viola. Optimal digital dynamical decoupling for general decoherence via walsh modulation. *Quantum Information Processing*, 16(11):1–18, 2017.

[72] Friedemann Reinhard, Fazhan Shi, Nan Zhao, Florian Rempp, Boris Naydenov, Jan Meijer, Liam T Hall, Lloyd Hollenberg, Jiangfeng Du, Ren-Bao Liu, et al. Tuning a spin bath through the quantum-classical transition. *Physical Review Letters*, 108(20):200402, 2012.

[73] G Robinson. Logical convolution and discrete walsh and fourier power spectra. *IEEE Transactions on Audio and Electroacoustics*, 20(4):271–280, 1972.

[74] Björn T Rosner and Daniel W Van Der Weide. High-frequency near-field microscopy. *Review of Scientific Instruments*, 73(7):2505–2525, 2002.

[75] Maximilian Schlosshauer. Decoherence, the measurement problem, and interpretations of quantum mechanics. *Reviews of Modern physics*, 76(4):1267, 2005.

[76] Thomas Sebastian, Katrin Schultheiss, Björn Obry, Burkard Hillebrands, and Helmut Schultheiss. Micro-focused brillouin light scattering: imaging spin waves at the nanoscale. *Frontiers in Physics*, 3:35, 2015.

[77] Alexandre M Souza, Gonzalo A Alvarez, and Dieter Suter. Robust dynamical decoupling for quantum computing and quantum memory. *Physical Review Letters*, 106(24):240501, 2011.

[78] Tobias Staudacher, Fazhan Shi, S Pezzagna, Jan Meijer, Jiangfeng Du, Carlos A Meriles, Friedemann Reinhard, and Joerg Wrachtrup. Nuclear magnetic resonance spectroscopy on a (5-nanometer) 3 sample volume. *Science*, 339(6119):561–563, 2013.

[79] Youngkyu Sung, Félix Beaudoin, Leigh M Norris, Fei Yan, David K Kim, Jack Y Qiu, Uwe von Lüpke, Jonilyn L Yoder, Terry P Orlando, Simon Gustavsson, et al. Non-gaussian noise spectroscopy with a superconducting qubit sensor. *Nature Communications*, 10(1):1–8, 2019.

[80] Dieter Suter and Gonzalo A Álvarez. Colloquium: Protecting quantum information against environmental noise. *Reviews of Modern Physics*, 88(4):041001, 2016.

[81] Dieter Suter and Fedor Jelezko. Single-spin magnetic resonance in the nitrogen-vacancy center of diamond. *Progress in Nuclear Magnetic Resonance Spectroscopy*, 98:50–62, 2017.

[82] Piotr Szańkowski and Łukasz Cywiński. Accuracy of dynamical-decoupling-based spectroscopy of gaussian noise. *Physical Review A*, 97(3):032101, 2018.

[83] Piotr Szańkowski, Guy Ramon, Jan Krzywda, Damian Kwiatkowski, et al. Environmental noise spectroscopy with qubits subjected to dynamical decoupling. *Journal of Physics: Condensed Matter*, 29(33):333001, 2017.

[84] Piotr Szańkowski, Marek Trippenbach, and Łukasz Cywiński. Spectroscopy of cross correlations of environmental noises with two qubits. *Physical Review A*, 94(1):012109, 2016.

[85] TH Taminiau, JJT Wagenaar, T Van der Sar, Fedor Jelezko, Viatcheslav V Dobrovitski, and R Hanson. Detection and control of individual nuclear spins using a weakly coupled electron spin. *Physical Review Letters*, 109(13):137602, 2012.

[86] JM Taylor, Paola Cappellaro, L Childress, Liang Jiang, Dmitry Budker, PR Hemmer, Amir Yacoby, R Walsworth, and MD Lukin. High-sensitivity diamond magnetometer with nanoscale resolution. *Nature Physics*, 4(10):810–816, 2008.

[87] George E Uhlenbeck and Leonard S Ornstein. On the theory of the brownian motion. *Physical Review*, 36(5):823, 1930.

[88] Götz S Uhrig. Keeping a quantum bit alive by optimized π-pulse sequences. *Physical Review Letters*, 98(10):100504, 2007.

[89] Götz S Uhrig. Exact results on dynamical decoupling by π pulses in quantum information processes. *New Journal of Physics*, 10(8):083024, 2008.

[90] Lorenza Viola and Emanuel Knill. Robust dynamical decoupling of quantum systems with bounded controls. *Physical Review Letters*, 90(3):037901, 2003.

[91] Lorenza Viola, Emanuel Knill, and Seth Lloyd. Dynamical decoupling of open quantum systems. *Physical Review Letters*, 82(12):2417, 1999.

[92] Lorenza Viola and Seth Lloyd. Dynamical suppression of decoherence in two-state quantum systems. *Physical Review A*, 58(4):2733, 1998.

[93] Guoqing Wang, Yi-Xiang Liu, Yuan Zhu, and Paola Cappellaro. Nanoscale vector ac magnetometry with a single nitrogen-vacancy center in diamond. *Nano Letters*, 21(12):5143–5150, 2021.

[94] Jacob R West, Daniel A Lidar, Bryan H Fong, and Mark F Gyure. High fidelity quantum gates via dynamical decoupling. *Physical Review Letters*, 105(23):230503, 2010.

[95] Emil Wolf. *Introduction to the Theory of Coherence and Polarization of Light*. Cambridge University Press, 2007.

[96] Tatsuro Yuge, Susumu Sasaki, and Yoshiro Hirayama. Measurement of the noise spectrum using a multiple-pulse sequence. *Physical Review Letters*, 107(17):170504, 2011.

[97] H Dieter Zeh. On the interpretation of measurement in quantum theory. *Foundations of Physics*, 1(1):69–76, 1970.

[98] Jingfu Zhang, Alexandre M Souza, Frederico Dias Brandao, and Dieter Suter. Protected quantum computing: interleaving gate operations with dynamical decoupling sequences. *Physical Review Letters*, 112(5):050502, 2014.

[99] Nan Zhao, Zhen-Yu Wang, and Ren-Bao Liu. Anomalous decoherence effect in a quantum bath. *Physical Review Letters*, 106(21):217205, 2011.